A&A, 696, A126 (2025)
https://doi.org/10.1051/0004-6361/202553811

Astronomy & Astrophysics

Analyses of anomalous lensing events detected from the UKIRT microlensing survey

Cheongho Han[1], Weicheng Zang[2,3], Andrzej Udalski[4], Chung-Uk Lee[5,⋆], Ian A. Bond[6], Yongxin Wen[7,8], Bo Ma[7,8], Michael D. Albrow[9], Sun-Ju Chung[5], Andrew Gould[10], Kyu-Ha Hwang[5], Youn Kil Jung[5], Yoon-Hyun Ryu[5], Yossi Shvartzvald[12], In-Gu Shin[2], Hongjing Yang[3], Jennifer C. Yee[2], Doeon Kim[1], Dong-Jin Kim[5], Sang-Mok Cha[5,11], Seung-Lee Kim[5], Dong-Joo Lee[5], Yongseok Lee[5,11], Byeong-Gon Park[5], Richard W. Pogge[10],
(The KMTNet Collaboration)
Przemek Mróz[4], Michał K. Szymański[4], Jan Skowron[4], Radosław Poleski[4], Igor Soszyński[4], Paweł Pietrukowicz[4], Szymon Kozłowski[4], Krzysztof A. Rybicki[4,12], Patryk Iwanek[4], Krzysztof Ulaczyk[13], Marcin Wrona[4,14], Mariusz Gromadzki[4], Mateusz J. Mróz[4],
(The OGLE Collaboration)
Fumio Abe[15], Ken Bando[20], David P. Bennett[16,17], Aparna Bhattacharya[16,17], Akihiko Fukui[18,19], Ryusei Hamada[20], Shunya Hamada[20], Naoto Hamasaki[20], Yuki Hirao[21], Stela Ishitani Silva[16,22], Naoki Koshimoto[20], Yutaka Matsubara[15], Shota Miyazaki[23], Yasushi Muraki[15], Tutumi Nagai[20], Kansuke Nunota[20], Greg Olmschenk[16], Clément Ranc[24], Nicholas J. Rattenbury[25], Yuki Satoh[20], Takahiro Sumi[20], Daisuke Suzuki[20], Sean K. Terry[16,17], Paul J. Tristram[26], Aikaterini Vandorou[16,17], and Hibiki Yama[20]
(The MOA Collaboration)

(Affiliations can be found after the references)

Received 20 January 2025 / Accepted 18 March 2025

ABSTRACT

Aims. The United Kingdom Infrared Telescope (UKIRT) microlensing survey was conducted over four years, from 2016 to 2019, with the goal of serving as a precursor to future near-infrared microlensing surveys. Focusing on stars in the Galactic center and utilizing near-infrared passbands, the survey identified approximately one thousand microlensing events, 27 of which displayed anomalies in their light curves. This paper presents an analysis of these anomalous events, aiming to uncover the underlying causes of the observed anomalies.

Methods. The events were analyzed under various configurations, considering the potential binarity of both the lens and the source. For 11 events that were additionally observed by other optical microlensing surveys, including those conducted by the OGLE, KMTNet, and MOA collaborations, we incorporated their data into our analysis.

Results. Among the reported anomalous events, we revealed the nature of 24 events except for three events, in which one was likely to be a transient variable, and two were difficult to accurately characterize their nature due to the limitations of the available data. We confirmed the binary lens nature of the anomalies in 22 events. Among these, we verified the earlier discovery that the companion in the binary lens system UKIRT11L is a planetary object. Accurately describing the anomaly in UKIRT21 required a model that accounted for the binarity of both the lens and the source. For two events UKIRT01 and UKIRT17, the anomalies could be interpreted using either a binary-source or a binary-lens model. For the UKIRT05, it was found that accounting for higher-order effects induced by the orbit al motions of both Earth and the binary lens was crucial. With the measured microlensing parallax togeter with the angular Einstein radius, the component masses of the UKIRT05 binary lens were determined to be $M_1 = (1.05 \pm 0.20)\,M_\odot$, $M_2 = (0.36 \pm 0.07)\,M_\odot$, and the distance to the lens was found to be $D_L = (3.11 \pm 0.40)$ kpc.

Key words. gravitational lensing: micro

1. Introduction

A microlensing survey was conducted over four years, from 2016 to 2019, using the United Kingdom Infrared Telescope (UKIRT) to observe stars in the Galactic center in the near-infrared (NIR) passband (Shvartzvald et al. 2017). The survey targeted the Galactic center field, reaching $l = b = 0°$, a region difficult to observe with optical lensing surveys such as the Korea Microlensing Telescope Network (KMTNet; Kim et al. 2016), the Optical Gravitational Lensing Experiment (OGLE; Udalski 2015), and the Microlensing Observations in Astrophysics (MOA; Bond et al. 2001; Sumi et al. 2003). The primary objective of the UKIRT survey was to examine the spatial

⋆ Corresponding author; leecu@kasi.re.kr

variation in microlensing event rates across the Galactic center field. The results from this survey provide valuable insights to refine and optimize future NIR microlensing surveys, including those planned for the Nancy Grace Roman Space Telescope (Spergel et al. 2015), by enhancing predictions and detections of microlensing events in densely populated, dust-obscured regions of the sky.

During the four-year survey period, the UKIRT microlensing survey identified a total of 985 microlensing events. Of these, 522 were definitively classified as single-lens single-source (1L1S) events, where the flux of a single source star was gravitationally magnified by a single-mass lens. An additional 436 events were categorized as probable 1L1S events, which are considered likely microlensing events despite not meeting all classification criteria. Detailed lensing parameters for these 1L1S events are provided in Table A1 of Wen et al. (2023).

In addition to the standard 1L1S events, Wen et al. (2023) identified 27 candidate anomalous events with light curves that deviated from the smooth and symmetric profiles typical of 1L1S events. These deviations suggest more complex lensing configurations, but detailed analyses of these anomalous events have not yet been conducted, leaving their exact nature uncertain.

Some of these events are likely binary-lens single-source (2L1S) events, with the anomalies resulting from the source star crossing the caustic structures created by the binary lens system. Such caustic crossings typically generate sharp and distinct features in the light curve. For events without clear caustic-crossing signatures, their origins remain ambiguous, potentially involving alternative lensing configurations, such as single-lens binary-source (1L2S) systems. Further analysis will be essential to classify these events and uncover the physical mechanisms underlying their anomalous features.

In this paper, we present detailed analyses of the anomalous microlensing events detected by the UKIRT microlensing survey. We first examine the binary nature of both the lens and the source by modeling the light curves using binary-lens and binary-source configurations. If these models fail to fully account for the anomalies, we investigate more complex scenarios by incorporating additional lens or source components into the 2L1S and 1L2S configurations.

The paper is organized as follows. Section 2 provides a detailed description of the data used in our analyses. For UKIRT events with additional data from other lensing surveys, we incorporated all available datasets to ensure a comprehensive analysis. A list of these events, along with the corresponding additional data, is also included for reference. In Section 3, we discuss the primary causes of anomalies in lensing light curves and outline the parameters required for modeling such anomalies. Additionally, we explain the procedure of the lensing modeling conducted to find a set of lensing parameters that best describe observed light curves. Section 4 focuses on the modeling process for each individual anomalous lensing event. We describe the specific characteristics of the anomalies observed in each event, provide a detailed explanation of the modeling procedure, and present the results derived from the modeling. In Section 5, we estimate the angular Einstein radii for events with light curves showing finite-source effects and available I- and V-band photometry. We summarize results and conclude in Section 6.

2. Data

The UKIRT microlensing event data analyzed in this study were obtained from lensing survey conducted using the UKIRT telescope. The telescope has a 2.8-meter aperture and is equipped with the Wide Field Camera, featuring a pixel scale of 0.4″ and a field of view of approximately 0.8 deg^2 (Shvartzvald et al. 2017). Observations were carried out in two near-infrared passbands, H and K, with the data processed using the CASU multi-aperture photometry pipeline (Irwin et al. 2004; Hodgkin et al. 2009). The UKIRT survey fields vary depending on the observation year but are consistently located near the Galactic center, within a Galactic latitude of $b < 3°$, extending to $l = b = 0°$. This design serves the survey's primary objective of examining the spatial variation in microlensing event rates across the Galactic center observation field.

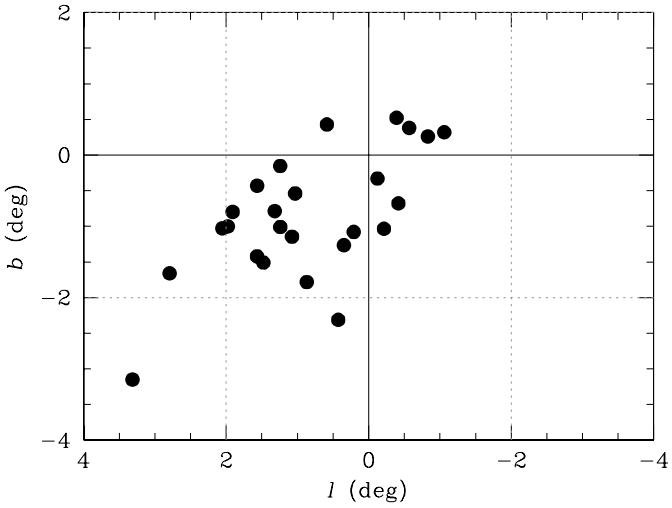

Fig. 1. Positions of anomalous events found by the UKIRT survey in Galactic coordinates.

Among the 27 anomalous transients with light curves deviating from the 1L1S lensing form, 26 were identified as lensing events, with the exception of UKIRT03, which is likely a variable star. The positions of these anomalous UKIRT events in Galactic coordinates are shown in Figure 1, while their Equatorial coordinates are provided in Paper I. Of the reported anomalous events, 11 were also observed by other optical microlensing surveys conducted by the OGLE, KMTNet, and MOA groups. Table 1 lists the events observed by multiple surveys, along with the identification references assigned by each survey group. In this work, we use the UKIRT references to designate the events.

Data from the other lensing surveys were obtained using their respective instruments. The OGLE survey is carried out using a 1.6-meter telescope equipped with a camera covering a 1.4 square-degree field, located at Las Campanas Observatory in Chile. The KMTNet survey employs a network of three identical 1.6-meter telescopes situated at geographically distributed sites: Siding Spring Observatory in Australia (KMTA), Cerro Tololo Inter-American Observatory in Chile (KMTC), and the South African Astronomical Observatory in South Africa (KMTS). Each KMTNet telescope is fitted with a camera that provides a 4 square-degree field of view. Meanwhile, the MOA survey operates a 1.8-meter telescope at Mt. John University Observatory in New Zealand, equipped with a camera covering a 2.2 square-degree field. Observations from OGLE and KMTNet were primarily performed in the I-band, while the MOA survey utilized a custom MOA-R band, spanning wavelengths from 609 to 1109 nm. The data from these additional surveys were reduced using photometry pipelines specific to each survey group: the OGLE data were processed with the pipeline developed by Udalski (2003), the KMTNet data were analyzed using

Table 1. Event coordinates and correspondence.

UKIRT	$(RA, Dec)_{J2000}$	OGLE	KMTNet	MOA
UKIRT-01	(17:54:25.15, –27:42:01.6)	–	–	–
UKIRT-02	(18:05:34.12, –27:39:39.1)	OGLE-2016-0BLG-562	KMT-2016-BLG-0042	–
UKIRT-03	(17:58:17.28, –28:40:52.2)	–	–	–
UKIRT-04	(17:58:33.87, –27:22:43.6)	OGLE-2016-BLG-0887	KMT-2016-BLG-0617	–
UKIRT-05	(17:54:50.52, –28:19:07.1)	–	KMT-2016-BLG-0180	–
UKIRT-06	(17:50:20.87, –29:18:55.6)	OGLE-2016-BLG-0262	KMT-2016-BLG-0592	–
UKIRT-07	(17:53:11.35, –27:42:32.6)	–	–	–
UKIRT-08	(17:42:45.92, -29:13:15.1)	–	–	–
UKIRT-09	(17:47:17.25, –29:38:43.4)	–	–	–
UKIRT-10	(17:49:10.47, –29:39:20.4)	–	–	–
UKIRT-11	(17:46:36.98, –29:12:40.9)	–	–	–
UKIRT-12	(17:49:08.63, –27:57:09.5)	–	–	–
UKIRT-13	(17:54:08.71, –27:45:16.9)	–	–	–
UKIRT-14	(17:54:58.96, –28:26:21.8)	OGLE-2017-BLG-1323	KMT-2017-BLG-0213	MOA-2017-BLG-431
UKIRT-15	(17:51:24.11, –29:17:27.7)	OGLE-2017-BLG-1471	KMT-2017-BLG-0318	MOA-2017-BLG-423
UKIRT-16	(17:45:20.79, –28:12:43.7)	–	–	–
UKIRT-17	(17:50:58.26, –27:49:00.1)	–	–	–
UKIRT-18	(17:52:28.43, –28:23:35.4)	OGLE-2018-BLG-0752	postseason	–
UKIRT-19	(17:52:37.79, –28:36:14.1)	OGLE-2018-BLG-1055	KMT-2018-BLG-2095	–
UKIRT-20	(17:51:46.70, –28:12:42.1)	OGLE-2018-BLG-0856	KMT-2018-BLG-2392	–
UKIRT-21	(17:41:49.39, –29:40:15.7)	–	–	–
UKIRT-22	(17:42:36.48, –29:30:21.9)	–	–	–
UKIRT-23	(17:42:39.02, –28:59:40.8)	–	–	–
UKIRT-24	(17:41:27.98, –29:00:02.8)	–	–	–
UKIRT-25	(17:50:08.93, –28:19:52.9)	–	–	–
UKIRT-26	(17:55:44.43, –29:45:10.5)	OGLE-2019-BLG-0950	KMT-2019-BLG-1326	MOA-2019-BLG-277
UKIRT-27	(17:54:39.34, –29:06:14.7)	OGLE-2019-BLG-1048	KMT-2019-BLG-1450	MOA-2019-BLG-363

the method described by Albrow et al. (2009), and the MOA data were reduced following the approach outlined by Bond et al. (2001). In the modeling process, we adjusted the error bars of the data to match the data scatter and to ensure that the χ^2 per degree of freedom for each data set equals unity, following the procedure outlined in Yee et al. (2012).

3. Lensing model

The lensing magnification of a 1L1S event depends on the projected separation between the lens and the source, normalized to the angular Einstein radius (θ_E), following the relation:

$$A = \frac{u^2+2}{u(u^2+4)^{1/2}}; \qquad u = \left[u_0^2 + \left(\frac{t-t_0}{t_E}\right)^2\right]^{1/2}. \tag{1}$$

Here, t_0 represents the time at the closest approach between the lens and the source, and u_0 (normalized to θ_E) indicates the separation at t_0 (impact parameter). The parameter t_E denotes the event timescale, defined as the time it takes the source to traverse the Einstein ring radius. As a result, modeling the light curve of a 1L1S event requires three lensing parameters: (t_0, u_0, t_E). The resulting lensing light curve is smooth and symmetric about t_0 (Paczyński 1986).

A lensing light curve may deviate from the standard 1L1S form due to various factors, with the binarity of the lens being the most common cause (Mao & Paczyński 1991). In 2L1S events, the lensing system creates a caustic structure on the source plane, which represents locations at which the lensing magnification of a point source becomes infinite. As a result, 2L1S light curves show deviations from the 1L1S form when the source approaches or crosses the caustic. The shape, size, and position of the caustic vary depending on the projected separation between the lens components (s, normalized to θ_E) and their mass ratio (q) (Cassan 2008). Anomalies caused by caustic crossings are affected by finite-source effects. In the case of an extended source event, the observed magnification is determined by the intensity-weighted amplification averaged over the surface of the source star (Nemiroff & Wickramasinghe 1994; Witt & Mao 1994; Bennett & Rhie 1996; Gould & Gaucherel 1997). Consequently, finite-source effects smooth out the sharp caustic spikes in the lensing light curves. The presence of a caustic structure introduces four additional parameters, (s, q, α, ρ), necessary for modeling a 2L1S event. Here, α denotes the angle between the source motion direction and the binary-lens axis, while ρ represents the ratio of the angular source radius (θ_*) to θ_E (normalized source radius).

Another important cause of deviations from the 1L1S form is the binarity of the source. In a 1L2S event, the lensing light curve is the combined result of the contributions from the events associated with each individual source star (Griest & Hu 1992; Di Stefano & Esin 1995; Han & Gould 1997; Dominik 1998). As a result, the light curve exhibits deviations from the smooth, single-peak profile characteristic of a 1L1S event. Modeling the light curve of 1L2S events requires three additional parameters to describe the source companion: $(t_{0,2}, u_{0,2}, q_F)$. Here, $(t_{0,2}, u_{0,2})$ represent the impact parameter and approach time of the second source, while q_F denotes the flux ratio between the secondary and primary source stars. If the light curve is influenced by the

finite size of the second source, an additional parameter, ρ_2, representing the normalized radius of the second source, must be included in the modeling.

We initially modeled the anomalous UKIRT events using the most common lens configurations, 2L1S and 1L2S systems. The goal of the modeling is to identify the set of lensing parameters (lensing solution) that best describe the observed light curves. For the 2L1S system, we first search for the binary parameters (s, q) using a grid approach with multiple starting values of α, while the other parameters are explored through a downhill method. Subsequently, we refine the solution by allowing all parameters to vary. For the 1L2S configuration, we determine the lensing solution by considering the location and magnitude of the anomaly in the light curve.

In some rare instances where anomalies in lensing light curves are challenging to describe precisely with a 2L1S or a 1L2S model, we employed more complex modeling. We consider two scenarios, with the first being a 3L1S configuration where the lens is a triple system and the source is a single star, as exemplified by the lensing event KMT-2021-BLG-1122 (Han et al. 2023), and the second being a 2L2S configuration where both the lens and the source are binaries, as demonstrated in the events KMT-2021-BLG-0284, KMT-2022-BLG-2480, and KMT-2024-BLG-0412 (Han et al. 2024).

For events with long timescales and well-sampled light curves, we conducted additional modeling to account for higher-order effects that could impact the light curve. Specifically, we considered two effects: microlens parallax and lens orbital motion. The microlens-parallax effect arises from the movement of Earth in its orbit around the Sun, which leads to a shift in the observer's position (Gould 1992). On the other hand, the lens-orbital effect is caused by the motion of the binary lens components in orbit around their common center of mass, which also results in a positional change of the lens system (Batista et al. 2011; Skowron et al. 2011). The modeling considering the microlens-parallax effect requires two additional parameters, $(\pi_{\mathrm{E},N}, \pi_{\mathrm{E},E})$, which correspond to the north and east components of the microlens-parallax vector $\boldsymbol{\pi}_{\mathrm{E}}$. The direction of the microlens-parallax vector aligns with that of the relative lens-source proper motion vector $(\boldsymbol{\mu})$, and its magnitude is related to the relative lens-source parallax (π_{rel}) by $\pi_{\mathrm{E}} = \pi_{\mathrm{rel}}/\theta_{\mathrm{E}}$. To first-order approximation, the lens orbital motion is described by two parameters, $(ds/dt, d\alpha/dt)$, which represent the annual rates of change in the binary separation and the source trajectory angle, respectively (Albrow et al. 2002; Jung et al. 2013).

4. Lens-system configuration

In this section, we present the results of modeling the individual anomalous UKIRT lensing events. For each event, we provide the lensing solution and describe the corresponding lens-system configuration. In cases where multiple solutions arise due to degeneracies, we present all possible solutions and explain the cause of the degeneracy. Lensing solutions are provided for 24 of the 26 anomalous UKIRT lensing events, with the exception of UKIRT10 and UKIRT24, for which accurate characterization is difficult due to the limitations of the available data.

4.1. UKIRT01

Figure 2 presents the lensing light curve of UKIRT01, which occurred in the 2016 observing season. This source of the event, located at Galactic coordinates $(l, b) = (2^\circ.0545, -1^\circ.0277)$, was exclusively monitored by the UKIRT survey, as it lay outside the coverage areas of other surveys. Observations during the 2016 season were conducted in a single passband, H, with two data points collected daily to track the event. The light curve peaked around May 12, 2016, corresponding to the reduced heliocentric Julian date (HJD′) ≡ HJD 2 450 000 ∼ 7522.2.

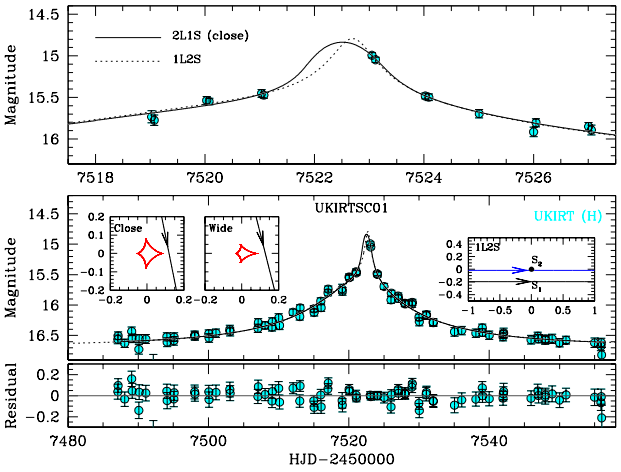

Fig. 2. Lensing light curve of UKIRT01. The lower panel displays the full view of the light curve, while the upper panel provides a zoomed-in view of the anomalous region. The insets in the lower panel illustrate the lens system configurations for the 2L1S model (left two insets) and the 1L2S solution (right inset). In the 2L1S configuration, the red closed curve represents the caustic, and the arrowed line indicates the source trajectory. In the 1L2S solution, the lens position is marked by a filled dot at the origin, while the blue and black arrowed lines represent the trajectories of the primary (S_1) and secondary (S_2) source stars, respectively.

The two data points recorded on HJD′ = 7523 exhibit deviations from the 1L1S form. Modeling the event with a 2L1S configuration revealed two solutions arising from the well-known close-wide degeneracy. In this degeneracy, one solution corresponds to a binary separation greater than unity ($s > 1$, "wide" solution), while the other corresponds to a separation less than unity ($s < 1$, "close" solution). The degeneracy between these solutions is notable, with $\Delta\chi^2 = 0.3$. Figure 2 displays the model curve for the close solution along with its residuals. The wide solution exhibits a very similar profile. The lens system configurations, showing the source trajectory relative to the caustic produced by the binary lens, are illustrated in the inner two insets of the lower panel. The full lensing parameters for both 2L1S solutions are listed in Table 2. The estimated mass ratio between the binary lens components is $q \sim 0.44$ for the close solution and $q \sim 0.19$ for the wide solution. In both cases, the anomaly is attributed to the source's passage through the extended perturbation region created by the protruding central caustic.

It is found that the anomaly can also be explained by a model with a 1L2S configuration. The model curve for the 1L2S solution is shown as a dotted line in Figure 2, and the corresponding model parameters are listed in Table 2. Under the 1L2S interpretation, the anomaly arises from the close approach of the faint companion of the source to the lens. The estimated flux ratio between the source companion and the primary source is $q_F \sim 0.16$. The lens system configuration is shown in the right inset of the lower panel.

4.2. UKIRT02

The event UKIRT02 was detected by the UKIRT survey during the 2016 observation season and was also observed by the OGLE

Table 2. Lensing parameters of UKIRT01.

Parameter	2L1S		1L2S
	Close	Wide	
χ^2	89.5	89.8	89.5
t_0 (HJD′)	7522.07 ± 0.12	7521.88 ± 0.12	7521.225 ± 0.255
u_0	0.123 ± 0.043	0.111 ± 0.027	0.193 ± 0.097
t_E (days)	21.05 ± 6.39	27.79 ± 9.67	24.17 ± 6.86
s	0.438 ± 0.082	2.604 ± 0.813	–
q	0.33 ± 0.16	0.19 ± 0.69	–
α (rad)	4.489 ± 0.055	4.459 ± 0.061	–
ρ (10^{-3})	–	–	–
$t_{0,2}$ (HJD′)	–	–	7522.700 ± 0.119
$u_{0,2}$ (HJD′)	–	–	0.015 ± 0.023
q_F	–	–	0.159 ± 0.050

Table 3. Best-fit parameters of UKIRT02, UKIRT04, UKIRT05, UKIRT06, and UKIRT07.

Parameter	UKIRT02	UKIRT04	UKIRT05	UKIRT06	UKIRT07
χ^2	6685.6	7472.2	6497.8	7722.9	136.9
t_0 (HJD′)	7492.893 ± 0.012	7536.53 ± 0.21	7548.00 ± 0.22	7515.929 ± 0.013	7556.38 ± 0.45
u_0	0.1508 ± 0.0025	0.8232 ± 0.0073	0.0628 ± 0.0017	0.1229 ± 0.0019	0.0952 ± 0.0088
t_E (days)	20.64 ± 0.12	27.20 ± 0.13	93.98 ± 0.21	74.66 ± 1.37	104.96 ± 6.10
s	1.6593 ± 0.0018	1.6251 ± 0.0048	1.5272 ± 0.0021	4.421 ± 0.056	0.981 ± 0.023
q	0.982 ± 0.022	0.374 ± 0.012	0.3320 ± 0.0025	1.114 ± 0.093	0.238 ± 0.024
α (rad)	4.6733 ± 0.0050	5.0613 ± 0.0081	3.1955 ± 0.0028	5.7136 ± 0.0019	0.058 ± 0.022
ρ (10^{-3})	0.957 ± 0.014	0.996 ± 0.016	0.5780 ± 0.0043	–	2.98 ± 0.49
$\pi_{E,N}$	–	–	−0.091 ± 0.010	–	–
$\pi_{E,E}$	–	–	0.068 ± 0.008	–	–
ds/dt	–	–	0.099 ± 0.025	–	–
$d\alpha/dt$	–	–	−0.429 ± 0.022	–	–

and KMTNet surveys, which designated it as OGLE-2016-BLG-0562 and KMT-2016-BLG-0042, respectively. The event was located within KMTNet's prime fields BLG03 and BLG43, both observed with a 0.5-hour cadence, providing an effective combined cadence of 0.25 hours. This resulted in a densely sampled light curve.

Figure 3 presents the lensing light curve of UKIRT02, which exhibits clear caustic-crossing features at HJD′ ∼ 7490.1 and 7495.8. The second caustic crossing was resolved by a combination of the OGLE and KMTC data sets. From the 2L1S modeling, we identified a unique solution with binary-lens parameters $(s, q) \sim (1.65, 0.98)$, indicating that the event was caused by a binary lens with nearly equal-mass components. The complete lensing parameters are provided in Table 3, and the model curve is overlaid on the data points in Figure 3.

The inset in the lower panel illustrates the lens system configuration, revealing that the binary lens generated a single resonant caustic elongated along the binary axis. The source traversed the left side of the caustic nearly vertically, producing the first spike at the caustic entrance and the second spike at the exit. The measured event timescale is $t_E \sim 21$ days, and the normalized source radius, $\rho \sim 0.96 \times 10^{-3}$, was derived from the resolved caustic.

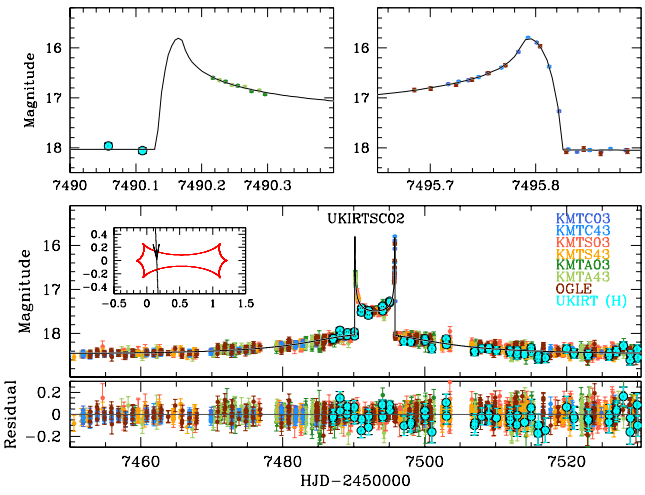

Fig. 3. Lensing light curve of UKIRT02. The notations are the same as in Fig. 2.

4.3. UKIRT04

The microlensing event UKIRT04 was the third anomalous event discovered by the UKIRT survey during the 2016 observing season. The source star of the event was located within the overlapping coverage regions of the OGLE and KMTNet surveys. The event IDs for these surveys are OGLE-2016-BLG-562 and KMT-2016-BLG-0042, respectively. Specifically, the source was situated in KMTNet's primary fields, BLG03 and BLG43, which were observed at a high cadence of 0.25 hours.

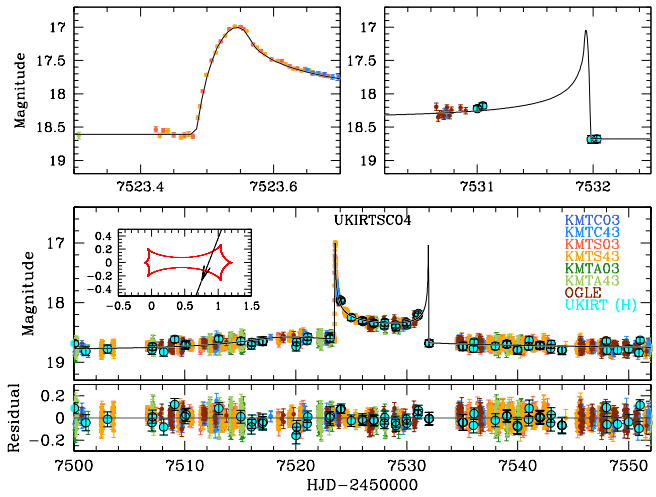

Fig. 4. Lensing light curve of UKIRT04.

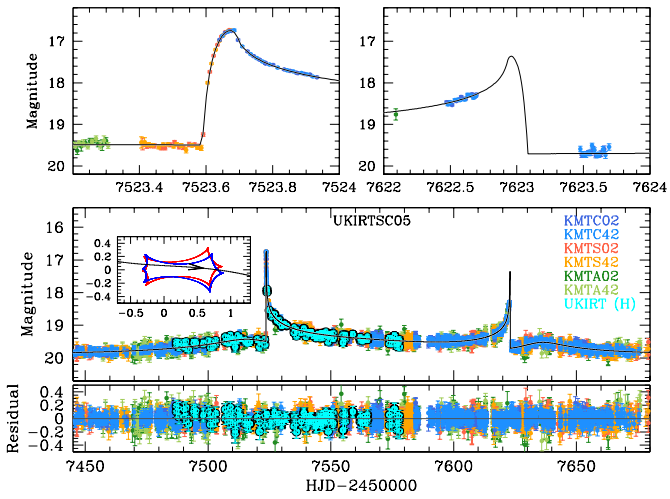

Fig. 5. Lensing light curve of UKIRT05. The two sets of caustics, depicted in red and blue in the inset of the lower panel, correspond to the caustics at the times of the first and second caustic crossings, respectively.

Figure 4 displays the light curve of UKIRT04, constructed by combining data from the three survey groups. Similar to UKIRT02, the light curve exhibits two distinct caustic spikes, with a U-shaped profile between them. The first spike, occurring at HJD′ ∼ 7523.55, was observed in the KMTC data set. Although the second caustic crossing was not directly resolved, it is estimated to have occurred at HJD′ ∼ 7531.95, based on the rising slope of the U-shaped profile preceding the crossing. Modeling the event using the 2L1S configuration yields binary lens parameters $(s, q) \sim (1.63, 0.37)$ and an event timescale of $t_{\rm E} \sim 27$ days. The normalized source radius, determined from the resolved caustic, was found to be $\rho \sim 1.00 \times 10^{-3}$. The full lensing parameters of the solution are listed in Table 3.

The configuration of the lens system is illustrated in the inset of the lower panel. The caustic shape is similar to that of UKIRT02, with a single resonant caustic elongated along the binary lens axis. One key difference is that the source crosses the right side of the caustic at a diagonal angle.

4.4. UKIRT05

The microlensing event UKIRT05, which occurred during the 2016 season, was observed by both the UKIRT and KMTNet surveys. In the KMTNet survey, the event was designated as KMT-2016-BLG-0180 and monitored with a high cadence of 0.25 hours. This event persisted throughout the entire 2016 bulge season, with the UKIRT survey covering approximately the first half of the event. In contrast, the KMTNet survey provided continuous observations spanning the full duration of the bulge season, ensuring comprehensive coverage of the light curve.

Figure 5 presents the lensing light curve of UKIRT05. Similar to the two previous events, the light curve displays characteristic caustic crossing features, consisting of two spikes with a U-shaped trough between them. The first caustic spike, occurring at HJD′ ∼ 7523.65, was resolved by combined data from the KMTC and KMTS. Although the second spike was not directly observed, it is estimated to have occurred around HJD′ ∼ 7622.9, based on the light curve profile before and after the spike. In addition to these caustic spikes, the light curve shows a weak bump around HJD′ ∼ 7645, which appears after the second spike.

Taking into account the caustic features, we performed modeling using the 2L1S configuration. Given the long duration of the event, we also included higher-order effects in the modeling. This approach yields a unique solution with binary parameters $(s, q) \sim (1.53, 0.33)$. As expected from the event's extended duration, the estimated event timescale, $t_{\rm E} \sim 94$ days, is notably long. The full set of lensing parameters for the solution is presented in Table 3. The model fit that incorporates higher-order effects is found to be significantly better (by $\Delta\chi^2 = 354.5$) compared to the fit from the model without these effects.

The inset of the lower panel of Figure 5 illustrates the configuration of the lens system. Due to the orbital motion of the lens, the caustics change over time, and we present two sets of caustics corresponding to the times of the first (red closed curve) and second (blue closed curve) caustic spikes. The lens system produces a single resonant caustic that is elongated along the binary lens axis, with the source crossing through the longer side of the caustic. This, combined with the long timescale, results in a 100-day time gap between the two caustic spikes. The weak bump after the second caustic spike arouse as the source approached the right side online cusp of the caustic.

4.5. UKIRT06

The event UKIRT06, occurred during the 2016 season, was observed not only by the UKIRT survey but also by two additional surveys conducted by the OGLE and KMTNet groups. Figure 6 shows the light curve of the event, with the peak brightness occurring around HJD′ ∼ 7516, at which point the source star brightened by approximately 1.7 magnitudes above its baseline level. The light curve around the peak exhibited a subtle anomaly that persisted for about 17 days. This anomaly is characterized by a negative deviation from the 1L1S model and displays a nearly plateau-like shape during its duration.

Choi et al. (2012) suggested that a plateau-shaped central anomaly can be produced either by a planetary companion located near the Einstein ring of the primary lens or by a binary companion positioned well beyond the Einstein ring. Based on this, we performed 2L1S modeling, systematically exploring the parameter space for both the planetary and binary regimes. From this modeling, we derived a solution indicative of a binary lens

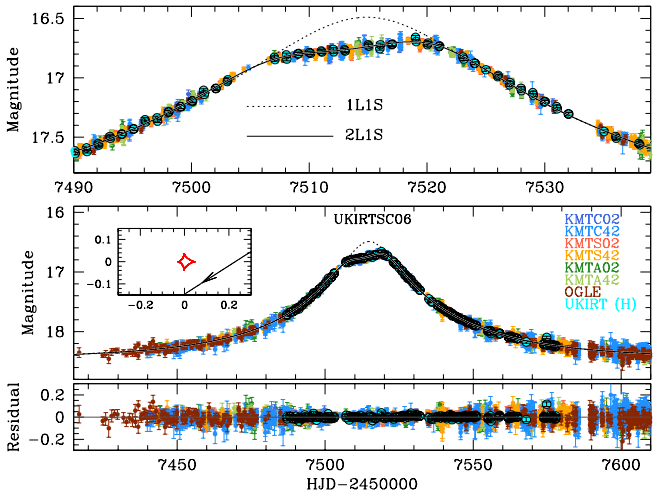

Fig. 6. Lensing light curve of UKIRT06. The dotted curve represents a 1L1S model derived by fitting the data while excluding the data points around the anomaly.

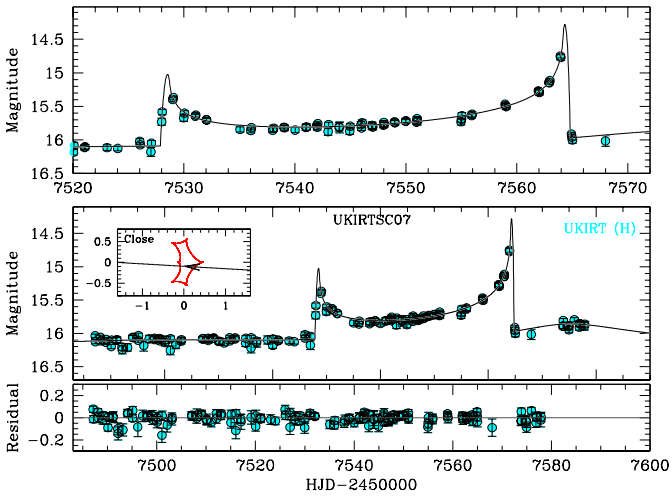

Fig. 7. Lensing light curve of UKIRT07.

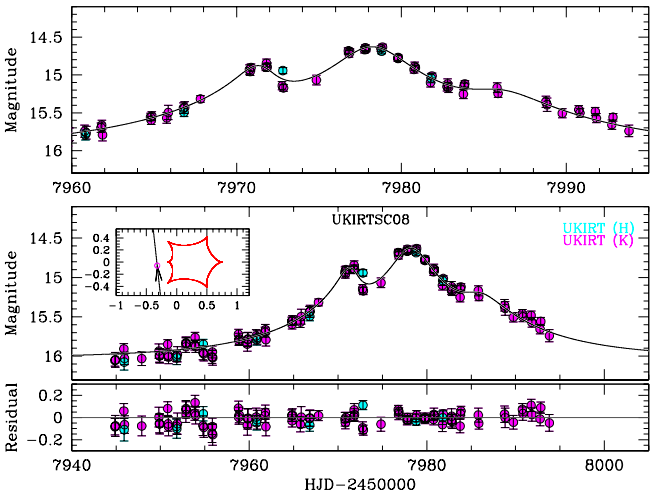

Fig. 8. Lensing light curve of UKIRT08.

system, with parameters $(s, q) \sim (4.4, 1.1)$. The complete set of lensing parameters for this solution is provided in Table 3.

The model light curve corresponding to the solution is overlaid on the observed data points in Figure 6. The lens system configuration for this solution is illustrated in the inset of the lower panel. The configuration shows that the anomaly was caused by the source passing through the negative anomaly region located outside one fold of the caustic.

4.6. UKIRT07

The source of the event, located near the Galactic center at coordinates, $(l, b) = (1^\circ.9091, -0^\circ.7973)$, resides in a region not covered by other optical lensing surveys. Consequently, it was observed exclusively by the UKIRT survey during the 2016 season.

The light curve of UKIRT07, shown in Figure 7, clearly displays caustic-crossing features, with two prominent spikes: one occurring at HJD′ ∼ 7528 and the other at HJD′ ∼ 7564. Additionally, a weaker bump is observed after the second caustic spike, centered around HJD′ ∼ 7585. Despite the low cadence of the survey, the first caustic spike was partially covered, which allowed for the estimation of the normalized source radius.

Modeling the light curve of the event using a 2L1S configuration yielded a solution with binary parameters of $(s, q) \sim (0.98, 0.24)$. The model curve of the solution is plotted in Figure 7. The binary separation is very close to the angular Einstein radius, leading to the formation of a resonant caustic, as shown in the inset of the lower panel. The source crossed the caustic nearly horizontally along the binary lens axis. The weak bump following the second caustic spike was caused by the source's close approach to the left-side on-axis cusp of the caustic. The event has a relatively long timescale of $t_{\rm E} \sim 105$ days, but determining higher-order lensing parameters was challenging due to the sparse and incomplete coverage of the light curve.

4.7. UKIRT08

UKIRT08 was the first anomalous lensing event detected during the 2017 season by the UKIRT survey. Observations during this season were conducted in two passbands, H and K. The source of UKIRT08 is located near the Galactic center, with Galactic coordinates $(l, b) \sim (-0^\circ.5691, 0^\circ.3823)$. This field lies outside the coverage of other optical lensing surveys, making the UKIRT survey the only one to observe the event. Observations for the season concluded at HJD′ = 7981, before the event had fully returned to its baseline.

Figure 8 shows the lensing light curve of UKIRT08. While it does not display caustic-crossing features, it is characterized by three consecutive bumps, centered at HJD′ ∼ 7971, 7979, and 7986. This anomaly pattern closely resembles that of the 2L1S lensing event KMT-2023-BLG-0601, identified through the KMTNet lensing survey (Han et al. 2024). In the KMT-2023-BLG-0601 event, three closely spaced bumps were observed as the source passed nearly vertically along one side of a caustic, approaching three successive cusps. This suggests that an anomaly characterized by three consecutive bumps is likely caused by a binary lens.

Given the likely binary-lens origin of the anomaly, we conducted a 2L1S modeling of the light curve. This analysis resulted in a solution with binary parameters $(s, q) \sim (1.24, 0.35)$. The lens system configuration, displayed in the inset of the lower panel, shows the formation of a single resonant caustic. As anticipated, based on the previous case with a similar anomaly

Table 4. Best-fit parameters of UKIRT08, UKIRT09, UKIRT11, UKIRT12, and UKIRT13.

Parameter	UKIRT08	UKIRT09	UKIRT11	UKIRT12	UKIRT13
χ^2	273.9	346.0	512.0	36.1	206.8
t_0 (HJD′)	7977.87 ± 0.10	7954.31 ± 7.14	7916.281 ± 0.058	7916.471 ± 0.091	7981.653 ± 0.080
u_0	0.325 ± 0.032	0.890 ± 0.041	4.01 ± 0.22	4.68 ± 0.56	6.23 ± 0.14
t_E (days)	16.14 ± 1.30	103.64 ± 9.63	79.70 ± 2.37	40.25 ± 1.59	120.34 ± 3.04
s	1.237 ± 0.060	1.559 ± 0.046	1.0144 ± 0.0069	3.72 ± 0.13	3.468 ± 0.079
q	0.345 ± 0.021	0.101 ± 0.087	$(1.88 \pm 0.18) \times 10^{-3}$	2.38 ± 0.84	5.903 ± 1.015
α (rad)	1.462 ± 0.019	4.311 ± 0.055	0.579 ± 0.018	3.467 ± 0.048	−0.1951 ± 0.0069
ρ (10^{-3})	–	–	9.10 ± 0.80	–	–

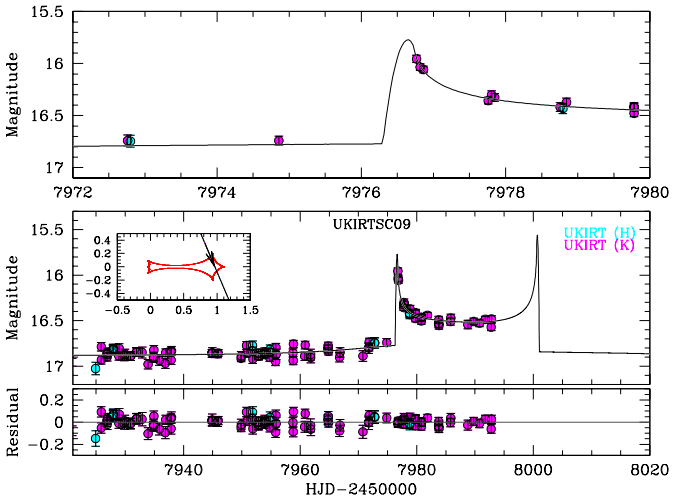

Fig. 9. Lensing light curve of UKIRT09.

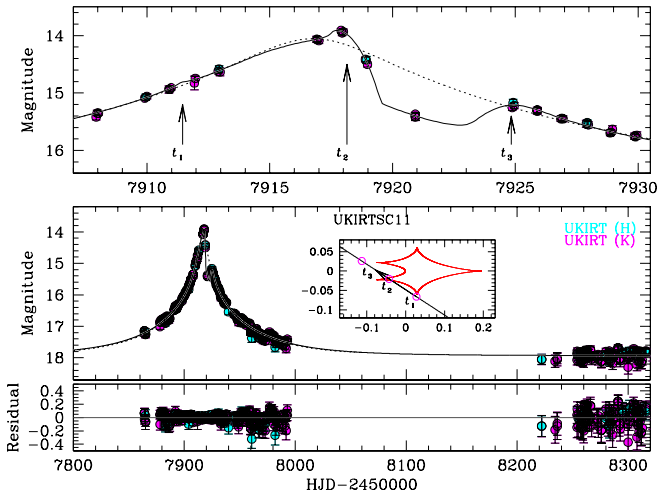

Fig. 10. Lensing light curve of UKIRT11. In the inset of the lower panel, the three empty circles on the source trajectory, labeled t_1, t_2, and t_3, represent the source positions at the times of consecutive approaches to the caustic cusps. The size of each circle is scaled to the size of the source. The times corresponding to these positions are indicated in the light curve by arrows. The dotted curve in the top panel represents a 1L1S model derived by excluding the data points around the anomaly.

pattern, the three anomaly features were caused by the vertical passage of the source through one side of the caustic. Table 4 provides the complete set of lensing parameters for the solution, excluding the normalized source radius, which could not be constrained.

4.8. UKIRT09

The lensing event UKIRT09, with its source located at Galactic coordinates $(l, b) = (-0°.4171, -0°.6791)$, was observed exclusively by the UKIRT survey. Figure 9 shows the light curve of UKIRT09, observed during the 2017 season. It features a prominent caustic spike at HJD′ = 7976.5, marking the source's entry into the caustic. However, the expected spike at the caustic exit was not observed, as it occurred after the observing season concluded, at HJD′ = 7989.

Despite the incomplete coverage of the light curve, a 2L1S modeling provided a unique solution with binary parameters of approximately $(s, q) \sim (1.56, 0.10)$ and a timescale of $t_E \sim 104$ days. The complet set of the lensing parameters are provided in Table 4.

The lower panel of Figure 9 includes an inset showing the lens system configuration. The caustic structure consists of two distinct components: a smaller caustic near the more massive lens component and a larger caustic on the side of the lower-mass lens component, separated by approximately $\Delta u \sim 0.9$. These two caustics are connected by a narrow bridge. The caustic spike occurred as the source passed through the larger caustic associated with the lighter lens component. According to the model, another spike was expected at HJD′ ∼ 8001, roughly 12 days after the observing season concluded.

4.9. UKIRT11

The lensing event UKIRT11, with its source situated very close to the Galactic center at Galactic coordinates $(l, b) = (-0°.1218, -0°.3291)$, was exclusively observed by the UKIRT survey during the 2017 season. Figure 10 presents the lensing light curve for the event. The source of this lensing event experienced a substantial magnification, with its peak brightness reaching roughly 4 magnitudes above the baseline level. Such a high-magnification event is especially sensitive to perturbations from a planetary companion to the lens, as pointed out by Griest & Safizadeh (1998). The light curve indeed showed a short-term anomaly near the event's peak. This anomaly exhibited both positive and negative deviations from the 1L1S model. The primary portion of the anomaly showed a negative deviation, flanked by weaker positive deviations on both sides of the main anomaly.

UKIRT11 is the only anomalous UKIRT lensing event that was previously analyzed in detail by Shvartzvald et al. (2018),

Table 5. Best-fit parameters of UKIRT14, UKIRT15, UKIRT16, and UKIRT17.

Parameter	UKIRT14	UKIRT15	UKIRT16	UKIRT17	
				2L1S	1L2S
χ^2	10629.2	9666.4	501.2	379.2	378.0
t_0 (HJD′)	7990.33 ± 0.25	7977.625 ± 0.025	8283.19 ± 0.31	8283.55 ± 0.43	8265.79 ± 0.27
u_0	0.60 ± 3.98	−1.307 ± 0.038	0.1176 ± 0.0074	0.160 ± 0.016	0.114 ± 0.021
t_E (days)	35.746 ± 0.062	65.69 ± 0.42	68.63 ± 3.86	168.33 ± 18.62	90.32 ± 11.17
s	1.77344 ± 0.00040	2.591 ± 0.012	0.67 ± 0.02	3.569 ± 0.065	–
q	1.056 ± 0.015	1.193 ± 0.036	0.691 ± 0.057	3.384 ± 1.063	–
α (rad)	2.6275 ± 0.0028	5.8339 ± 0.0042	3.494 ± 0.010	5.365 ± 0.012	–
ρ (10^{-3})	2.980 ± 0.024	2.120 ± 0.032	2.33 ± 0.33	–	–
$\pi_{E,N}$	−1.208 ± 0.049	–	–	–	–
$\pi_{E,E}$	0.133 ± 0.036	–	–	–	–
ds/dt	0.134 ± 0.132	–	–	–	–
$d\alpha/dt$	−1.325 ± 0.041	–	–	–	–
$t_{0,2}$	–	–	–	–	8298.29 ± 1.58
$u_{0,2}$	–	–	–	–	0.272 ± 0.078
q_F	–	–	–	–	1.29 ± 0.48

who reported that the companion in the binary lens system as a planetary object. Our modeling, utilizing the 2L1S configuration, independently confirmed that the anomaly arises from a planetary companion. The full set of lensing parameters for this solution is provided in Table 4. The derived planetary parameters, $(s, q) \sim (1.01, 1.9 \times 10^{-3})$, are in close agreement with the values $(s, q) \sim (1.03, 1.5 \times 10^{-3})$ reported by Shvartzvald et al. (2018).

The configuration of the lens system is depicted in the inset of the lower panel. The planet induces a resonant caustic, and the source passed close to this caustic multiple times. The source first approached the lower tip of the caustic at $t_1 = 7911.45$, then passed the lower-left cusp at $t_2 = 7918.15$, and later approached the upper-left cusp again at $t_3 = 7918.15$. The source positions at these individual cusp approaches are marked with empty circles labeled t_1, t_2, and t_3, with arrows indicating their corresponding positions in the light curve. The size of the circles is scaled to represent the size of the source relative to the caustic. The major dip anomaly occurred between t_2 and t_3. The bump at t_1, caused by the source's initial approach to the cusp, is relatively weak due to the combined effects of a faint cusp and significant finite-source effects.

4.10. UKIRT12

The lensing event UKIRT12, located at Galactic coordinates $(l, b) = (1°.243, -0°.1533)$, was observed exclusively by the UKIRT survey during the 2017 season, as it lies outside the coverage of the other surveys. Figure 11 shows the lensing light curve of the event, which reached a moderately high magnification at its peak, with the brightness increasing by approximately 3.2 magnitudes above the baseline. Although observations were interrupted by unfavorable weather over a four-day period from HJD′ = 7913 to 7916, the anomaly feature near the peak of the light curve is clearly discernible.

Modeling the light curve under a 2L1S configuration yielded a solution that well describe the anomaly feature. Unlike the event UKIRT11, the anomaly was turned out to be caused by a binary companion. The binary parameters of the solutions are $(s, q) \sim (3.7, 2.4)$, indicating that the companion has a mass greater than the lens component that the source approached and

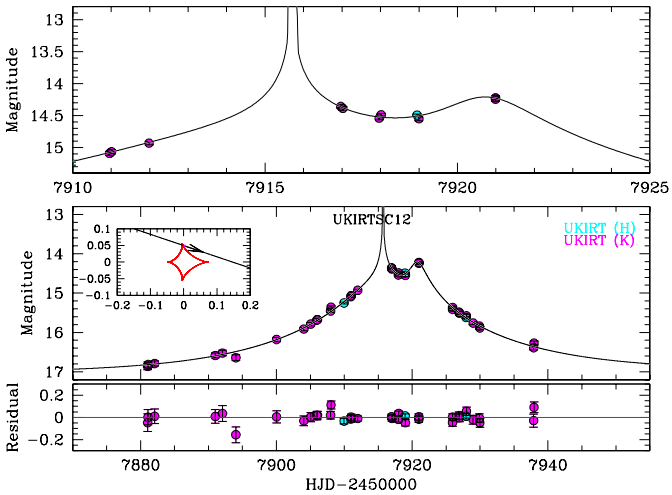

Fig. 11. Lensing light curve of UKIRT12.

it is positioned at a separation substantially greater than the Einstein radius. Table 4 provides the complete lensing parameters of the solution.

The inset in the lower panel of Figure 11 depicts the lens system configuration. The more massive binary lens companion generates a small diamond-shaped caustic near the position of the less massive lens component. The anomaly was caused by the source's diagonal passage through the vicinity of the caustic, first crossing the tip of the upper cusp and then approaching the on-axis cusp. The crossing of the first cusp produced a pronounced peak centered at around HJD′ = 7915.8, but this feature was not observed due to a gap in coverage.

4.11. UKIRT13

The lensing event UKIRT13, with its Galactic coordinates $(l, b) = (1°.9771, -1°.0028)$, was observed exclusively by the UKIRT survey conducted in the 2017 season Figure 12 shows the lensing light curve of the event. It exhibits a prominent anomaly centered at HJD′ = 7993, featuring strong positive deviations that exceed the baseline 1L1S model by about 1.7 magnitudes.

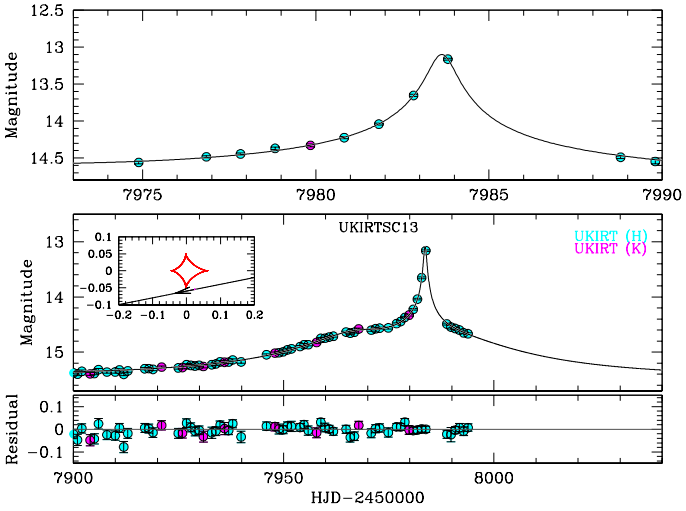

Fig. 12. Lensing light curve of UKIRT13.

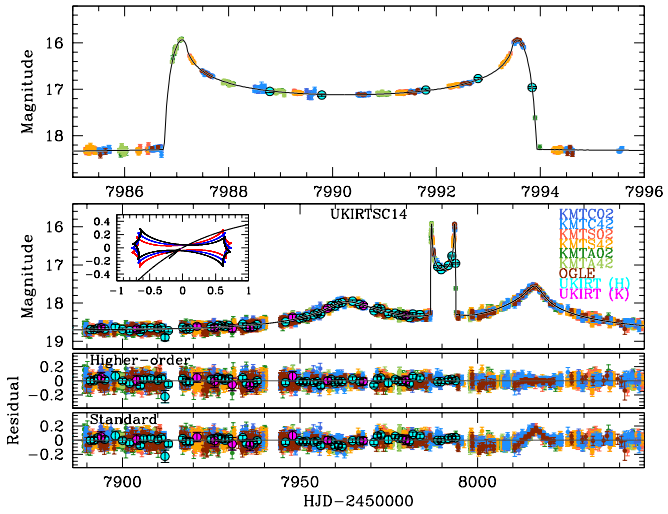

Fig. 13. Lensing light curve of UKIRT14. In the inset of the lower panel showing the lens-system configuration, the closed curves, marked in red, blue, and black, represent the caustics at HJD′ = 7960, 7990, and 8017, respectively. The bottom two panels display the residuals from the models obtained using two approaches, one that considers higher-order effects and the other that does not.

The 2017 season ended at HJD′ = 7993, and the light curve beyond this point was not covered.

The anomaly is well explained by a 2L1S model with binary lens parameters $(s, q) \sim (3.5, 5.9)$. The complete set of lensing parameters is provided in Table 4. The model curve corresponding to this solution is overlaid on the data points in Figure 12. The inset in the lower panel illustrates the lens system configuration. This event is similar to UKIRT12, as the anomaly resulted from the source approaching the caustic induced by a wide-separation binary lens companion, with the companion having a greater mass than the lens component approached by the source. The event has a relatively long timescale, $t_{\rm E} \sim 120$ days. However, determining higher-order lensing parameters was challenging due to incomplete coverage of the light curve during the latter part of the event.

4.12. UKIRT14

The source of the lensing event UKIRT14, located at Galactic coordinates $(l, b) = (1^\circ.4794, -1^\circ.5082)$, lies within the coverage of the three optical surveys conducted by the OGLE, KMTNet, and MOA groups conducted during the 2017 season. The event references designated by the individual surceys are OGLE-2017-BLG-1323, KMT-2017-BLG-0213, and MOA-2017-BLG-431. Figure 13 presents the lensing light curve of the event, which is constructed from the combined data sets, excluding the MOA data due to relatively large photometric uncertainties. The light curve displays several distinct features, including caustic-crossing spikes at HJD′ = 7987.0 and 7981.5, as well as two bumps linked to cusp approaches at HJD′ = 7962 and 8017. The final bump was not captured by the UKIRT survey because the 2017 season ended before it could be observed, but it was densely covered by the data from the other surveys.

Modeling the light curve reveals that the anomalies are well explained by a binary lens. The binary lens parameters are $(s, q) = (1.77, 1.06)$, indicating that the lens consists of approximately equal-mass components with a projected separation larger than the Einstein radius. It was found that incorporating higher-order effects is essential to accurately describe the anomaly features. This is evident from the comparison of residuals, shown in the two bottom panels of Figure 13, which were derived from two models – one accounting for higher-order effects and the other not. However, distinguishing between

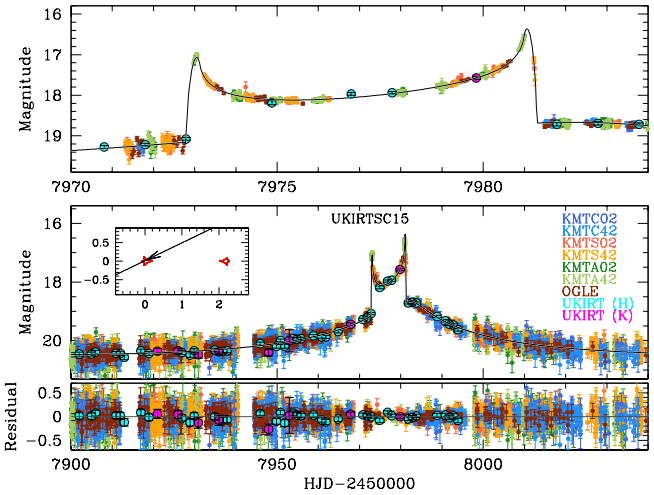

Fig. 14. Lensing light curve of UKIRT15.

microlens-parallax and lens-orbital effects proved difficult, as both introduce similar deviations in the light curves. This overlap complicates the precise determination of the higher-order parameters. The lensing parameters for one model are presented in Table 5, but it is important to note that multiple local solutions exist, all providing similarly good fits to the data.

The corresponding lens system configuration is illustrated in the inset of the lower panel. The caustic forms a resonant structure stretched along the binary axis. The source passed diagonally through the caustic, producing distinct caustic spikes. The two bumps, occurring before and after the caustic spikes, were caused by the source approaching the lower-left and upper-right cusps of the caustic, respectively.

4.13. UKIRT15

The lensing event UKIRT15 was observed during the 2017 season by the UKIRT survey as well as three additional optical

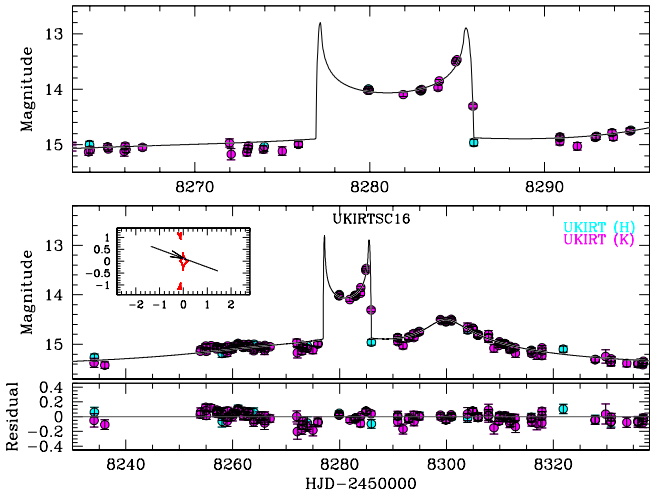

Fig. 15. Lensing light curve of UKIRT16.

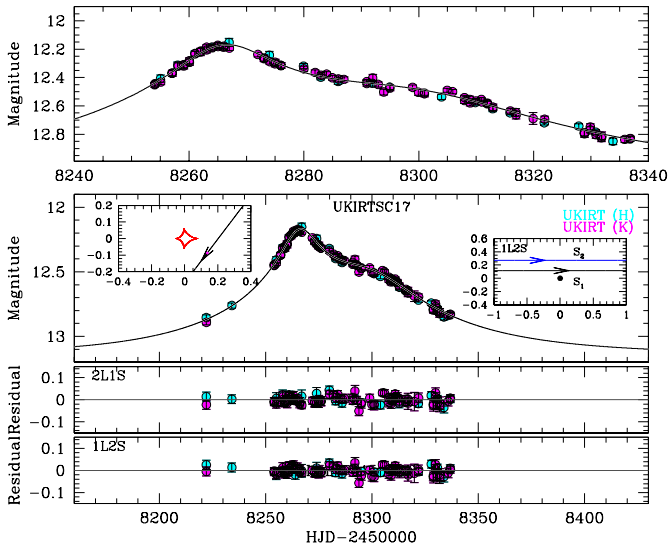

Fig. 16. Lensing light curve of UKIRT17. The model curves for the 2L1S and 1L2S models are superimposed on the data points, appearing indistinguishable within the thickness of the lines.

surveys: OGLE, KMTNet, and MOA. For this analysis, the MOA data set was excluded due to its relatively large uncertainties. The source position is within KMTNet's primary fields BLG02 and BLG43, toward which the event was monitored with a 0.25-hour cadence, resulting in dense light curve coverage. Figure 14 presents the lensing light curve of UKIRT15, constructed from the combined data sets. The light curve displays clear caustic-crossing features, with spikes at HJD′ = 7973.0 and 7981.1. Both caustic spikes were well-covered by the combined KMTA and KMTS data sets. The portions of the light curve not captured by the UKIRT data after HJD′ = 7993 were densely covered by data from the other surveys.

A 2L1S modeling of the light curve provides a unique solution characterized by the binary parameters $(s, q) \sim (2.6, 1.2)$ and an event timescale of $t_{\rm E} \sim 66$ days. Table 5 presents the full set of lensing parameters for the solution. The lens system configuration, illustrated in the inset of the lower panel in Figure 14, reveals that the binary lens creates two distinct sets of caustics, each located near one of the individual lens components. The source passed through the caustic associated with the lower-mass lens component, leading to the observed caustic spikes in the light curve.

4.14. UKIRT16

UKIRT16 was the first anomalous lensing event reported from the UKIRT survey during the 2018 season. The source of the event, located near the Galactic center with Galactic coordinates $(l, b) = (0.^\circ5866, 0.^\circ4287)$, resides in a region not covered by other surveys. Figure 15 presents the lensing light curve of UKIRT16, which exhibits caustic-crossing feature at HJD′ = 8285.7, followed by a bump around HJD′ = 8300. While not captured in the data, an additional caustic spike is inferred around HJD′ = 8276.8 from the extension of the U-shaped profile in the region between the observed caustic spikes.

Considering the caustic-related anomaly features, we performed 2L1S modeling of the light curve. The modeling yields a solution with binary parameters $(s, q) \sim (0.67, 0.69)$ and an event timescale of $t_{\rm E} \sim 69$ days. The complete set of lensing parameters is listed in Table 5. The normalized source radius is derived from the analysis of the caustic exit that was partially covered by the data. As shown in the inset of the lower panel, the lens system configuration reveals that the binary lens produced three sets of caustics, with one near the barycenter of the binary lens and two located farther away. The caustic features arise from the source passing through the central caustic.

4.15. UKIRT17

The source of the lensing event UKIRT17, with Galactic coordinates $(l, b) \sim (1.^\circ5664, -0.^\circ4300)$, lies in the region exclusively covered by the UKIRT survey during the 2018 season. The lensing light curve of the event is presented in Figure 16. It does not display a discontinuous anomaly but rather exhibits a smooth deviation from the 1L1S model.

Considering the characteristics of the anomaly, we carried out modeling using both the 2L1S and 1L2S models. The results show that the anomaly is explained almost equally well by both models, with $\chi^2 = 379.2$ for the 2L1S model and $\chi^2 = 378.0$ for the 1L2S model.

The lensing parameters for both models are listed in Table 5. The lens system configurations corresponding to the 2L1S and 1L2S solutions are illustrated in the left and right insets of the lower panel in Figure 16, respectively. Under the 2L1S solution, the lens is a binary characterized by $(s, q) \sim (2.6, 1.2)$, and the source passed through the outer region of a small caustic formed by the binary lens. In the 1L2S interpretation, the source is a binary consisting of two stars with a flux ratio of $q_F \sim 1.3$. The model curves for both solutions are superimposed on the data points, appearing indistinguishable within the thickness of the lines.

4.16. UKIRT18

The lensing event UKIRT18, located at Galactic coordinates $(l, b) = (1.^\circ2397, -1.^\circ0092)$, was observed during the 2018 season by the UKIRT, OGLE, and KMTNet surveys. The OGLE group designated the event as OGLE-2018-BLG-0752. Although the event was not initially detected in the KMTNet survey, and therefore no KMTNet ID was assigned, its photometric data was later retrieved through postseason photometry of the source.

Table 6. Best-fit parameters of UKIRT18, UKIRT19, UKIRT20, UKIRT21, and UKIRT22.

Parameter	UKIRT18	UKIRT19	UKIRT20	UKIRT21	UKIRT22	
					Close	Wide
χ^2	10617.9	10687.2	5650.6	598.5	621.8	609.8
t_0 (HJD′)	8257.756 ± 0.058	8285.770 ± 0.022	8266.86 ± 0.47	8621.474 ± 0.109	8664.786 ± 0.478	8665.801 ± 0.497
u_0	0.0280 ± 0.0036	0.4530 ± 0.0036	0.149 ± 0.015	0.0876 ± 0.0059	0.563 ± 0.012	0.664 ± 0.019
t_E (days)	38.99 ± 0.53	8.930 ± 0.034	137.95 ± 11.07	17.02 ± 0.85	38.18 ± 0.82	33.21 ± 0.73
s	0.8815 ± 0.0061	0.6274 ± 0.0012	0.50 ± 0.017	0.574 ± 0.019	0.8701 ± 0.0071	1.5005 ± 0.0064
q	1.444 ± 0.023	1.225 ± 0.045	0.442 ± 0.048	0.327 ± 0.054	0.311 ± 0.034	0.107 ± 0.017
α (rad)	2.190 ± 0.010	2.060 ± 0.013	3.313 ± 0.020	5.760 ± 0.025	2.379 ± 0.036	4.271 ± 0.023
ρ (10^{-3})	4.86 ± 0.23	8.31 ± 0.13	–	30.11 ± 3.47	11.66 ± 2.39	20.22 ± 2.00
$t_{0,2}$ (HJD′)	–	–	–	8635.488 ± 0.113	–	
$u_{0,2}$	–	–	–	−0.328 ± 0.042	–	
ρ_2 (10^{-3})	–	–	–	227.14 ± 19.69	–	
q_F	–	–	–	1.93 ± 0.23	–	

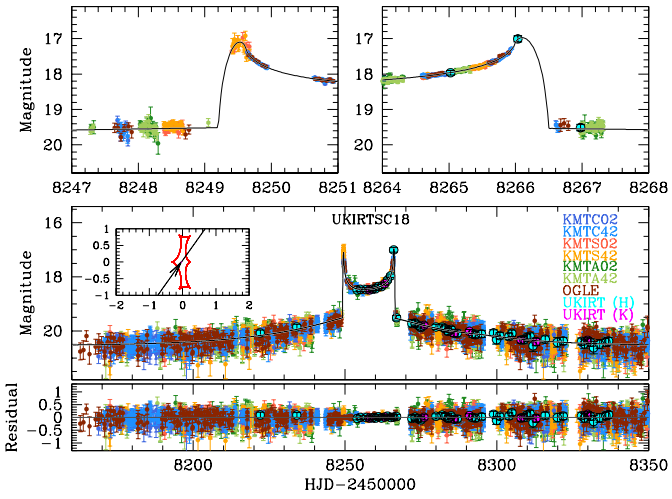

Fig. 17. Lensing light curve of UKIRT18. The two top panels show zoomed-in views of the sections during the source entrance and exit from the caustic.

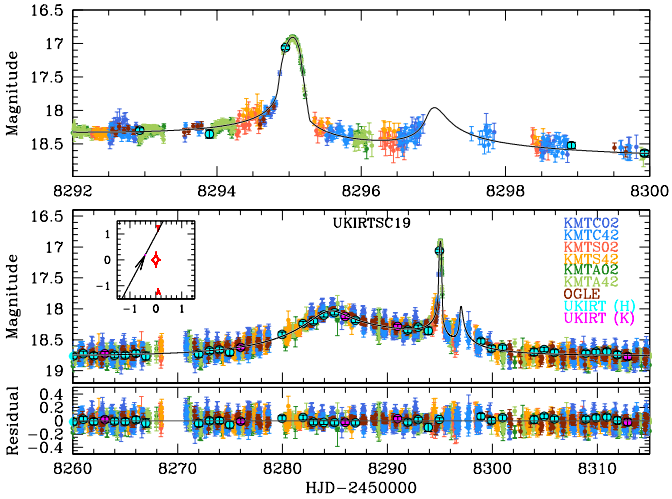

Fig. 18. Lensing light curve of UKIRT19.

Figure 17 displays the lensing light curve of UKIRT18, which was constructed by combining data from the UKIRT, OGLE, and KMTNet surveys. Although the observational cadence of the UKIRT survey was relatively low, the high cadences of the OGLE and KMTNet surveys allowed for a densely sampled light curve. This high-resolution data revealed intricate details of the light curve, including distinctive caustic-crossing features. The two spikes, centered at HJD′ ∼ 8249.5 and 8266.0, suggest the binary nature of the lens.

Modeling using the 2L1S configuration yields a unique solution with binary parameters $(s, q) \sim (0.88, 1.44)$ and an event timescale of $t_E \sim 39$ days. The complete set of lensing parameters for this solution is listed in Table 6. The corresponding model curve, which accurately fits the data, is overlaid on the data points in Figure 17. In the inset of the lower panel, both the caustic and the source trajectory are illustrated. The binary lens generates a resonant caustic that extends in a direction perpendicular to the binary axis. The source passes diagonally through this caustic, initially entering through the upper right fold and exiting via the lower left fold. The normalized source radius was determined by analyzing the data during the caustic crossing, which is well-resolved in the light curve.

4.17. UKIRT19

The lensing event UKIRT19, detected during the 2018 season, was also observed by the OGLE and KMTNet surveys, which designated the event as OGLE-2018-BLG-1055 and KMT-2018-BLG-2095, respectively. The light curve, constructed by combining data from the three surveys, is shown in Figure 18. It exhibits a relatively complex pattern, characterized by two successive positive deviations occurring at HJD′ ∼ 8295.0 and 8297.1, both appearing on the descending side of the curve. Since the maximum deviation of the first bump exceeds 1.5 magnitudes, it is likely that the anomaly was caused by a caustic crossing. Another noteworthy characteristic is that, excluding these anomalous features, the light curve is asymmetric.

From the 2L1S modeling, we obtain a unique solution that successfully explains all the observed anomaly features. The binary lens parameters of this solution are $(s, q) \sim (0.63, 1.23)$. The estimated event timescale, $t_E \sim 9$ days, is relatively short compared to other events. The complete set of lensing parameters is provided in Table 6. The model curve and residuals from the fit are shown in Figure 18. The lens system configuration, depicted in the inset of the lower panel, illustrates that the anomaly was caused by the source's approach to one of the two peripheral caustics formed by a binary lens with a separation

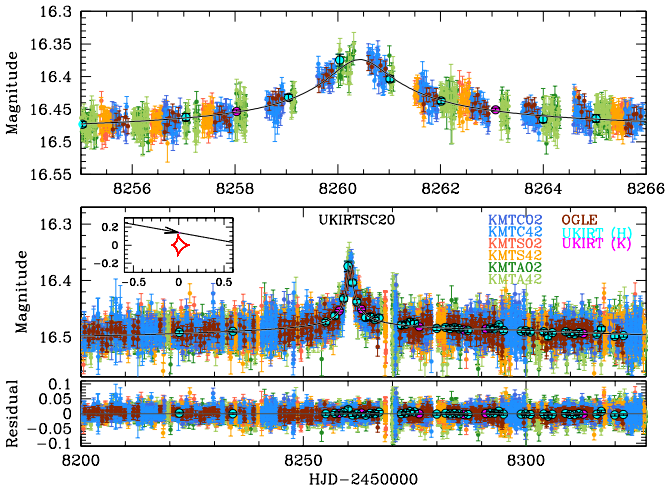

Fig. 19. Lensing light curve of UKIRT20.

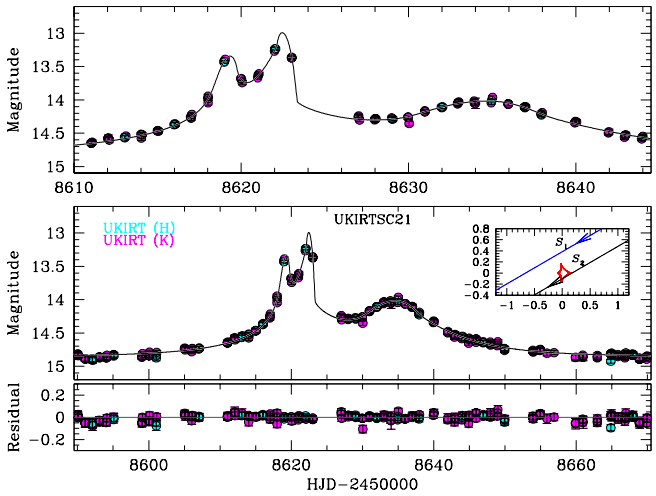

Fig. 20. Lensing light curve of UKIRT21.

smaller than the Einstein radius. The two bumps in the anomaly occur because the source passed near the two cusps of the three-cusp peripheral caustic.

4.18. UKIRT20

UKIRT20 is another lensing event commonly observed in the 2018 season by the three lensing surveys of the UKIRT, OGLE, and KMTNet. The ID references designated by the OGLE and KMTNet surveys are OGLE-2018-BLG-0856 and KMT-2018-BLG-2392, respectively. Figure 19 shows the lensing light curve of the event, showing that the source flux exhibited a rapid rise and fall during $8250 \lesssim \mathrm{HJD}' \lesssim 8260$, which were captured by the data from all three surveys. The source flux magnification due to lensing, excluding the anomaly, was small but persisted for a considerable duration.

The analysis reveals that the anomaly is well explained by a 2L1S model. The binary parameters for the solution are $(s, q) \sim (0.50, 0.44)$. As anticipated from the extended duration of the lensing magnification, the estimated event timescale, $t_{\rm E} \sim 138$ days, is relatively long compared to typical events. The complete set of lensing parameters is provided in Table 6, and the model curve corresponding to the solution is overlaid on the data points in Figure 19. The lens system configuration, shown in the inset of the lower panel, indicates that the binary lens produces a fold-fold caustic near the barycenter of the binary. The anomaly was caused by the source approaching the upper cusp of the caustic.

4.19. UKIRT21

UKIRT21 is the first anomalous lensing event detected during the 2019 season by the UKIRT survey. The source of the event is located near the Galactic center, with Galactic coordinates $(l, b) = (-1^\circ.0598, 0^\circ.3193)$, placing it outside the coverage of other optical lensing surveys. The lensing light curve of the event, shown in Figure 20, reveals multiple anomaly features. Between $\mathrm{HJD}' \sim 8617$ and $\mathrm{HJD}' \sim 8625$, the light curve displays characteristics indicative of caustic crossings. In addition to these features, the light curve also exhibits a bump centered at $\mathrm{HJD}' \sim 8635$.

Considering the caustic-crossing features, we initially modeled the light curve using a 2L1S configuration. However, this approach did not fully capture all the anomalous features. To explore the possibility that the caustic anomaly was caused by a binary lens, while the bump feature resulted from additional components in the lens or source system, we performed a second 2L1S modeling, excluding the region around the bump. This model effectively described the caustic-crossing portion of the light curve. Next, we introduced an additional source component, resulting in a binary-lens and binary-source (2L2S) system. This modeling provided a solution that accurately accounted for all the anomalies in the light curve. A subsequent 3L1S modeling did not yield a solution that matched the 2L2S model.

The model curve for the 2L2S solution is overlaid on the data points in the light curve, with the corresponding lensing parameters listed in Table 6. According to this solution, the lens is a binary system with parameters $(s, q) \sim (0.57, 0.33)$, creating a small four-cusp caustic near the barycenter of the binary lens, as shown in the inset of the lower panel. The source is also binary, consisting of two stars with a flux ratio of $q_F \sim 1.9$. The inset in the lower panel of Figure 20 illustrates the trajectories of the two source stars relative to the caustic. The caustic-related anomaly was caused by the fainter source star, which passed near the tip of the right-side on-axis cusp and then crossed the lower cusp. This sequence of caustic crossings, combined with significant finite-source effects, caused the anomaly to deviate from the typical caustic-crossing pattern. The bump feature, on the other hand, was produced by the approach of the brighter source star, which followed the fainter star and passed with a large impact parameter.

4.20. UKIRT22

The lensing event UKIRT22, which occurred during the 2019 season, was observed exclusively by the UKIRT survey, as its source is located near the Galactic center, with Galactic coordinates $(l, b) = (-0^\circ.8297, 0^\circ.2613)$, placing it in a region not covered by other surveys. Figure 21 presents the lensing light curve of the event, which shows caustic-crossing features. One spike is clearly visible at $\mathrm{HJD}' \sim 8671.9$, while the other caustic spike is not resolved by the data. The anomaly occurred during a period of low lensing magnification.

Modeling the light curve using a 2L1S configuration results in a pair of degenerate solutions: a close solution with $(s, q) \sim (0.87, 0.31)$ and a wide solution with $(s, q) \sim (1.50, 0.11)$. These solutions are referred to as "close" and "wide", depending on

Table 7. Best-fit parameters of UKIRT23, UKIRT25, UKIRT26, and UKIRT27.

Parameter	UKIRT23	UKIRT25	UKIRT26	UKIRT27
χ^2	656.6	483.9	10293.2	8090.5
t_0 (HJD′)	8598.88 ± 0.17	8624.79 ± 2.17	8670.9025 ± 0.0092	8709.621 ± 0.022
u_0	0.1050 ± 0.0017	0.590 ± 0.022	0.0606 ± 0.0008	0.2191 ± 0.0013
t_E (days)	59.27 ± 0.54	78.80 ± 2.35	8.427 ± 0.016	33.29 ± 0.14
s	1.5542 ± 0.0057	1.210 ± 0.017	1.3233 ± 0.0015	1.7303 ± 0.0026
q	0.925 ± 0.043	1.72 ± 0.32	0.3966 ± 0.0029	1.092 ± 0.011
α (rad)	2.7891 ± 0.0058	5.724 ± 0.036	−0.2459 ± 0.0006	5.1476 ± 0.0017
ρ (10^{-3})	5.97 ± 1.27	4.80 ± 0.55	16.001 ± 0.079	7.281 ± 0.045

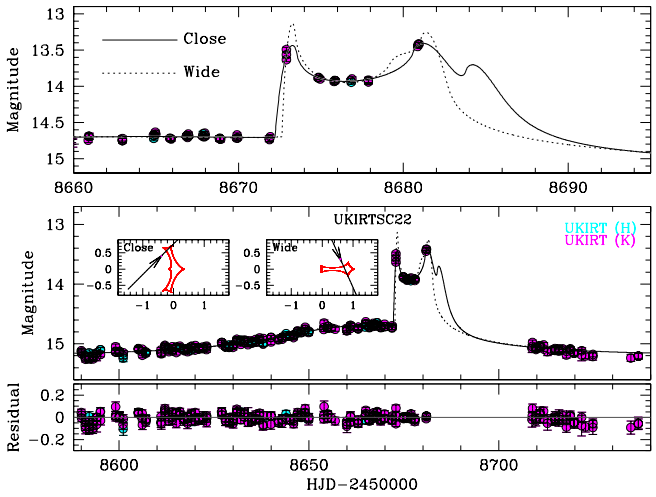

Fig. 21. Lensing light curve of UKIRT22. The two insets of the lower panel show the lens system configurations of the close and wide solutions.

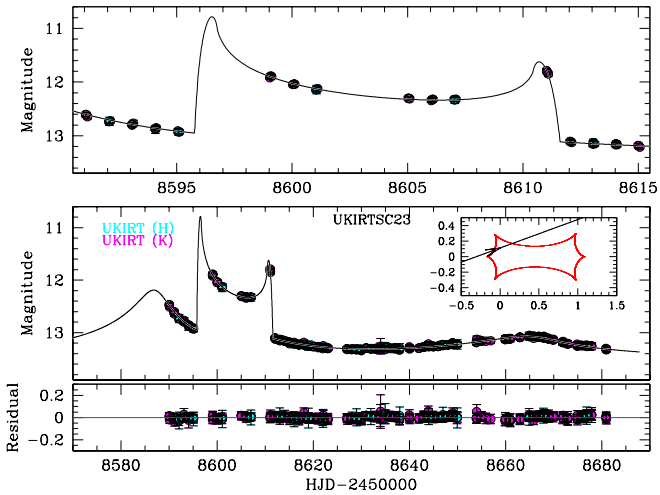

Fig. 22. Lensing light curve of UKIRT23.

whether the binary separation is smaller or larger than the Einstein radius, respectively. The model curves of the solutions are drawn over data points in Figure 21. The complete set of the lensing parameters are provided in Table 6. While the wide solution provides a slightly better fit, the difference in χ^2 values, $\Delta\chi^2 \sim 11.0$, is minor.

The lens system configurations for the close and wide solutions are shown in the inset of the lower panel of Figure 21. The caustics for both solutions exhibit a resonant structure, with the caustic of the close solution extending perpendicular to the binary lens axis, while that of the wide solution elongates along the axis. In both cases, the source crossed the edge of the caustic. After exiting, the source briefly crossed the tip of the caustic, resulting in a light curve profile that deviates from the typical caustic-crossing pattern.

4.21. UKIRT23

The source of the event UKIRT23, located near the Galactic center at Galactic coordinates $(l, b) = (-0°.3900, 0°.5227)$, was observed exclusively by the UKIRT survey conducted in the 2019 season. Figure 22 shows the lensing light curve of the event, which features prominent caustic-crossing signatures. The first unresolved caustic spike is estimated to have occurred around HJD′ ∼ 8696, while the second spike is observed at HJD′ ∼ 8611. In addition to these caustic-crossing features, the light curve shows two additional bumps, with a prominent one appearing before the first caustic spike and a weaker one centered near HJD′ ∼ 8666.

Modeling performed under the 2L1S lens system configuration yielded a unique solution that accurately reproduces all features of the anomaly. The binary parameters of the solution are $(s, q) \sim (1.55, 0.93)$, and the estimated timescale of the event is $t_E \sim 59$ days. Table 7 provides the complete set of lensing parameters. As illustrated in the lower panel of Figure 22, the lens system forms a resonant caustic extended along the binary lens axis. The source initially approached the left on-axis cusp, resulting in the first bump. It then entered the caustic by crossing the upper-left fold, producing the first caustic spike. Subsequently, the source exited the caustic by traversing the upper fold, which caused the second caustic spike. A final weak bump occurred as the source neared the upper-right cusp of the caustic.

4.22. UKIRT25

The lensing event UKIRT25, observed exclusively by the UKIRT survey, was detected during the 2019 season. Figure 23 presents the lensing light curve of the event, which shows a caustic-crossing feature around HJD′ ∼ 8608, with three data points capturing the first caustic spike. Although the duration of the caustic-related feature is relatively short, about 5 days, the anomaly is unlikely to result from a planetary companion, as the overall light curve deviates from the symmetric 1L1S profile. The occurrence of the caustic-related anomaly at low

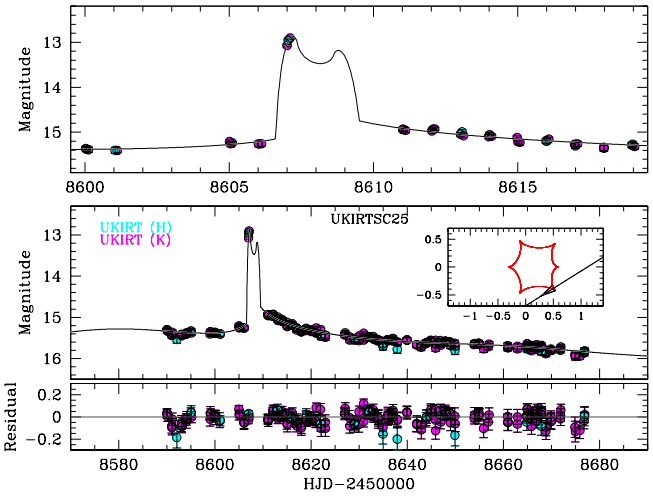

Fig. 23. Lensing light curve of UKIRT25.

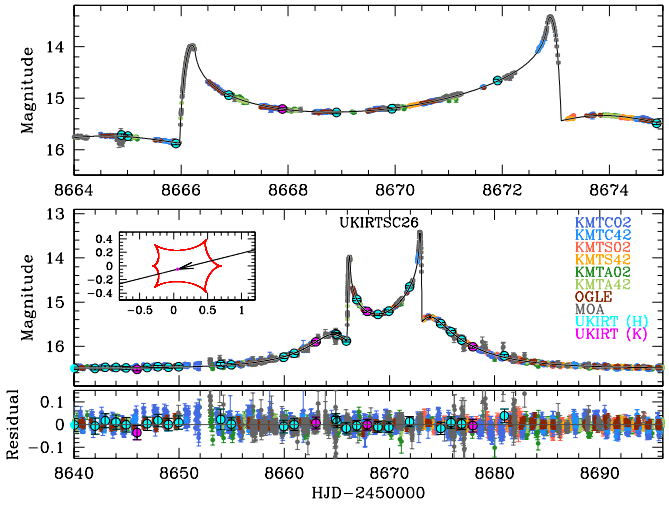

Fig. 24. Lensing light curve of UKIRT26.

magnification suggests that the source crossed a portion of the caustic located away from the barycenter of the binary lens.

Binary-lensing modeling has identified a solution that accurately accounts for the anomaly observed in the lensing light curve. The binary parameters corresponding to this solution are $(s, q) \sim (1.20, 1.72)$, with an event timescale of $t_{\rm E} \sim 79$ days. The complete set of lensing parameters associated with this model is detailed in Table 7. As illustrated in the inset of the lower panel, the lens system configuration demonstrates that the binary lens generates a resonant caustic characterized by six distinct cusps. The source trajectory passed the tip of the lower-right cusp, leading to the observed caustic-crossing anomaly, which occurred at a relatively low magnification. Furthermore, the asymmetry observed in the light curve results from the influence of the large caustic, which distorts the overall magnification pattern.

4.23. UKIRT26

The lensing event UKIRT26, which occurred in the 2019 season, was observed not only by the UKIRT survey but also by three optical lensing surveys conducted by the OGLE, KMTNet, and MOA groups. The source lies within the prime fields of these optical surveys, leading to a very dense coverage of the light curve, as shown in Figure 24. The light curve is characterized by well-resolved caustic-crossing features, with two distinct spikes observed at HJD′ ∼ 8666.1 and 8672.8. In addition to these spikes, weak bumps are present just before the first spike and after the second spike, adding further complexity to the structure of the light curve.

Through 2L1S modeling, we identified a unique solution that precisely describes the observed features of the light curve. The binary parameters associated with this solution are $(s, q) \sim (1.32, 0.40)$, and the event has a timescale of $t_{\rm E} \sim 8.4$ days. This makes it the shortest-duration event among the reported anomalous microlensing events. The complete set of lensing parameters derived from this model is presented in Table 7. Additionally, the model curve corresponding to this solution is superimposed on the observed data points in Figure 24.

As shown in the lens system configuration, presented in the inset of the lower panel, the binary lens forms a resonant caustic that extends along the binary lens axis. The source entered the caustic by crossing the upper-right fold and exited through the lower-left fold. The two weak bumps observed before and after

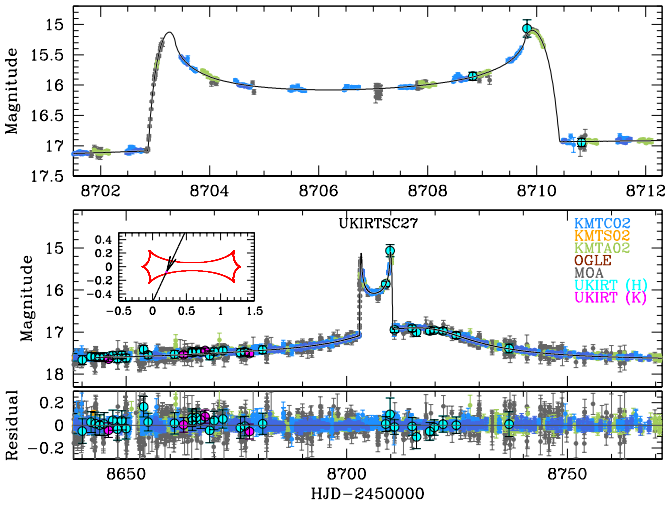

Fig. 25. Lensing light curve of UKIRT27.

the caustic spikes occurred as the source passed through regions of positive deviation formed near the on-axis cusps of the caustic. The normalized source radius was precisely determined from the resolved caustics.

4.24. UKIRT27

The UKIRT lensing survey concluded with the completion of the 2019 season, and UKIRT27 marks the final anomalous event reported from the survey. The source of the event lies in a region also monitored by other optical lensing surveys, including OGLE, MOA, and KMTNet. Figure 25 presents the lensing light curve of the event, which features prominent caustic-crossing spikes at HJD′ ∼ 8703.0 and 8710.2. The first caustic spike was resolved by the combined data from the MOA and KMTA datasets, while the second spike was covered by the KMTC, KMTA, and UKIRT H-band datasets. In addition to the caustic spikes, the light curve displays a weak bump following the second caustic crossing, before gradually returning to the baseline.

The anomalies in the lensing light curve are well described by a 2L1S model. The lensing parameters for this solution are provided in Table 7. The binary lens is defined by parameters

Table 8. Angular source radius, Einstein radius, and relative proper motion.

Event	$(V-I, I)_0$	θ_* (μas)	θ_E (mas)	μ (mas/yr)
UKIRT02	$(0.892 \pm 0.065, 18.252 \pm 0.020)$	0.862 ± 0.082	0.890 ± 0.086	15.89 ± 1.53
UKIRT04	$(0.753 \pm 0.082, 18.427 \pm 0.013)$	0.682 ± 0.073	0.131 ± 0.019	1.662 ± 0.251
UKIRT05	$(1.061 \pm 0.134, 18.661 \pm 0.020)$	0.86 ± 0.13	1.50 ± 0.23	5.84 ± 0.88
UKIRT14	$(0.931 \pm 0.043, 16.350 \pm 0.021)$	2.17 ± 0.18	0.73 ± 0.06	7.43 ± 0.61
UKIRT26	$(1.491 \pm 0.041, 15.038 \pm 0.020)$	6.24 ± 0.51	0.387 ± 0.032	16.85 ± 1.37
UKIRT27	$(1.194 \pm 0.045, 15.721 \pm 0.020)$	3.83 ± 0.32	0.529 ± 0.044	5.75 ± 0.48

$(s, q) \sim (2.73, 1.01)$, producing a resonant caustic that extends parallel to the binary lens axis. The event has an estimated timescale of $t_E \sim 33$ days.

The lens system configuration is illustrated in the inset of the lower panel of Figure 25. The source entered the caustic through the upper fold and exited via the lower fold, generating the distinct caustic spikes observed in the light curve. After the second spike, a weak bump was detected, caused by the source passing through a region of positive deviation near the lower-left cusp of the caustic. The normalized source radius was precisely measured by analyzing the resolved caustic crossings.

5. Angular Einstein radii

In this section, we determine the Einstein radii for events with well-resolved caustics and well-covered I- and V-band light curves. The process begins by measuring the instrumental (uncalibrated) I- and V-band magnitudes of the source by fitting the light curve data to the model curve. The light curve for measuring the source magnitude is constructed using the pydia software developed by Albrow (2017). The source is then placed on the instrumental (uncalibrated) color-magnitude diagram (CMD) of nearby stars, which is constructed using the same pydia code. To account for extinction and reddening, the source color and magnitude are calibrated using the centroid of the red giant clump (RGC) as a reference. For the dereddened color, $(V-I)_{RGC,0}$, and magnitude, $I_{RGC,0}$, of the RGC centroid, we adopt the values from Bensby et al. (2013) and Nataf et al. (2013), respectively. The calibrated $V-I$ color is then converted into a $V-K$ color using the color-color relation from Bessell & Brett (1988). The angular radius of the source (θ_*) is subsequently derived from the $(V-K)$–θ_* relation provided by Kervella et al. (2004). Finally, the Einstein radius is calculated using the angular source radius and the normalized source radius through the relation $\theta_E = \theta_*/\rho$. The relative lens-source proper motion is then determined as $\mu = \theta_E/t_E$, using the measured Einstein radius and the event timescale.

The Einstein radius was determined for six events: UKIRT02, UKIRT04, UKIRT05, UKIRT14, UKIRT26, and UKIRT27. For the remaining events, determining θ_E proved challenging due to several factors. Firstly, many events observed exclusively by the UKIRT survey had data in only a single passband, and even when observations were made in two bands, the light curve coverage in one of them was often inadequate for accurate color determination. Secondly, for some events with measured $H-K$ color, calibration was difficult due to the lack of prior dereddened values for the RGC, hindering its use as a reference. Thirdly, in most UKIRT-only events, the light curve did not display a caustic crossing, and when one occurred, it was not sufficiently resolved to determine ρ. Finally, even for events where the caustic was resolved through additional survey data, the quality of V-band data was often inadequate for color determination due to significant extinction in regions near the Galactic center.

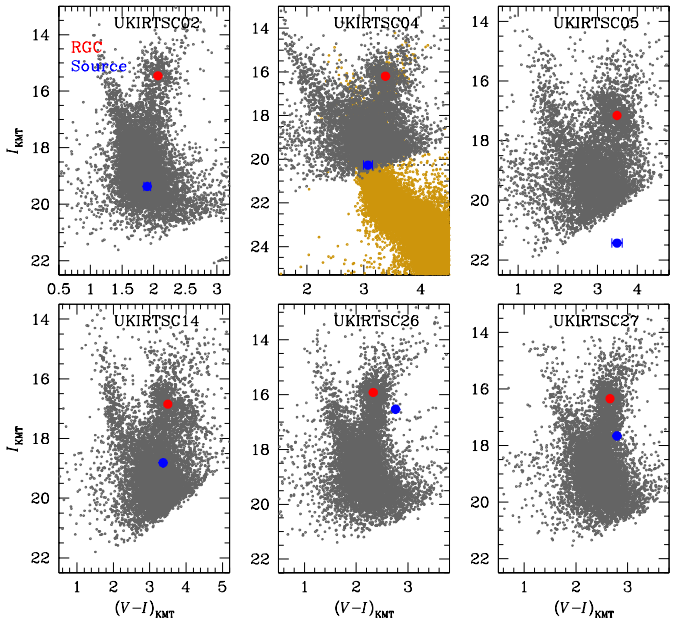

Fig. 26. Locations of source stars for the lensing events UKIRT02, UKIRT04, UKIRT05, UKIRT14, UKIRT26, and UKIRT27. The red filled dot in each panel represents the centroid of the red giant clump (RGC), which was used for calibrating the color and magnitude.

Figure 26 shows the locations of source stars for the six lensing events with measured Einstein radii. In the case of UKIRT04, for which the I-band source magnitude was determined but the V-band magnitude was not, we first aligned the CMD from ground-based observations with that obtained from HST observations (Holtzman et al. 1998). We then inferred the source color and magnitude as the mean values along the main-sequence branch. In Table 8, we listed the estimated values of the dereddened source color and magnitude, $(V-I, I)_0$, angular source radius, angular Einstein radius, and relative lens-source proper motion.

For the event UKIRT05, both the angular Einstein radius and the microlens parallax were measured. In this case, the physical parameters of the lens mass and the lens distance can be uniquely determined using the Gould (2000) relation:

$$M = \frac{\theta_E}{\kappa \pi_E}; \qquad D_L = \frac{\mathrm{AU}}{\pi_E \theta_E + \pi_S}. \tag{2}$$

Here $\kappa = 4G/(c^2 \mathrm{AU})$, $\pi_S = \mathrm{AU}/D_S$ represents the parallax of the source lying at a distance D_S. The estimated masses of the lens

components and distance are

$$M_1 = (1.21 \pm 0.21)\, M_\odot,$$
$$M_2 = (0.40 \pm 0.07)\, M_\odot, \quad (3)$$
$$D_L = (3.37 \pm 0.40)\ \mathrm{kpc}.$$

6. Summary and conclusion

We conducted an investigation into the anomalous microlensing events reported by the UKIRT microlensing survey, which was carried out over a period of four years, from 2016 to 2019. This survey primarily focused on observing stars near the Galactic center using near-infrared passbands, with the goal of examining how microlensing event rates vary spatially across the field of the Galactic center. In the analysis, we incorporated data from 11 microlensing events that were also observed by other optical microlensing surveys, including those conducted by the OGLE, KMTNet, and MOA collaborations.

Among the 27 anomalous events reported from the survey, we revealed the nature of 24 events except for three events, in which UKIRT03 was likely to be a transient variable, and UKIRT10 and UKIRT24 were were difficult to accurately characterize their nature due to the limitations of the available data. We have confirmed the binary lens nature of the anomalies for 21 events, including UKIRT02, UKIRT04, UKIRT05, UKIRT06, UKIRT07, UKIRT08, UKIRT09, UKIRT11, UKIRT12, UKIRT13, UKIRT14, UKIRT15, UKIRT16, UKIRT18, UKIRT19, UKIRT20, UKIRT22, UKIRT23, UKIRT25, UKIRT26, and UKIRT27. Among these binary lens events, the companion of UKIRT11L is a planetary object which has a mass ratio to its host of $(1.88 \pm 0.18) \times 10^{-3}$. For two events UKIRT01 and UKIRT17, the anomalies could be interpreted using either a binary-source or a binary-lens model. For the precise description of the anomaly in UKIRT21, it was needed a model where not only the lens and but also source are binaries.

For the events UKIRT05 and UKIRT14, it was found that accounting for higher-order effects induced by the orbital motions of both Earth and the binary lens was crucial. While accurately determining the higher-order parameters for UKIRT14 proved challenging due to the difficulty in distinguishing between microlens-parallax and lens-orbital effects, these parameters were securely measured for UKIRT05. With these measurements, along with the angular Einstein radius, the component masses of the UKIRT05 binary lens were determined to be $M_1 = (1.05 \pm 0.20)\, M_\odot$, $M_2 = (0.36 \pm 0.07)\, M_\odot$, and the distance to the lens was found to be $D_L = (3.11 \pm 0.40)$ kpc.

The UKIRT lensing experiment was primarily conducted to support the preparation of future lensing surveys with the Roman telescope. This study demonstrated that lensing events can be successfully detected even in the central regions of the Galaxy, where optical observations are challenging. However, the observational conditions, such as precision and cadence, differ between the UKIRT and Roman experiments. Moreover, the limited number of detected events in the UKIRT data makes it insufficient for statistically estimating the frequency of higher-order effects or the probability of events requiring complex modeling, such as 2L2S or 3L1S.

Acknowledgements. This research was supported by the Korea Astronomy and Space Science Institute under the R&D program (Project No. 2025-1-830-05) supervised by the Ministry of Science and ICT. This research has made use of the KMTNet system operated by the Korea Astronomy and Space Science Institute (KASI) at three host sites of CTIO in Chile, SAAO in South Africa, and SSO in Australia. Data transfer from the host site to KASI was supported by the Korea Research Environment Open NETwork (KREONET). This research was supported by the KASI under the R&D program (Project No. 2023-1-832-03) supervised by the Ministry of Science and ICT. The MOA project is supported by JSPS KAKENHI Grant Number JP24253004, JP26247023,JP16H06287 and JP22H00153. J.C.Y., I.G.S., and S.J.C. acknowledge support from NSF Grant No. AST-2108414. C.R. was supported by the Research fellowship of the Alexander von Humboldt Foundation. W. Zang and H.Y. acknowledge support by the National Natural Science Foundation of China (Grant No. 12133005). W. Zang acknowledges the support from the Harvard-Smithsonian Center for Astrophysics through the CfA Fellowship.

References

Albrow, M. 2017, https://doi.org/10.5281/zenodo.268049
Albrow, M. D., Beaulieu, J.-P., Caldwell, J. A. R., et al. 2000, ApJ, 534, 894
Albrow, M., Horne, K., Bramich, D. M., et al. 2009, MNRAS, 397, 2099
Batista, V., Gould, A., Dieters, S., et al. 2011, A&A, 529, A102
Bennett, D. P., & Rhie, S. H. 1996, ApJ, 472, 660
Bensby, T. Yee, J.C., Feltzing, S. et al. 2013, A&A, 549, A147
Bessell, M. S., & Brett, J. M. 1988, PASP, 100, 1134
Bond, I. A., Abe, F., Dodd, R. J., et al. 2001, MNRAS, 327, 868
Cassan, A. 2008, A&A, 491, 587
Choi, J.-Y., Shin, I.-G., Han, C., et al. 2012, ApJ, 756, 48
Di Stefano, R., & Esin, A. A. 1995, ApJ, 448, L1
Dominik, M. 1998, A&A, 333, 893
Gould, A. 1992, ApJ, 392, 442
Gould, A. 2000, ApJ, 542, 785
Gould, A., & Gaucherel, C. 1997, ApJ, 477, 580
Griest, K., & Hu, W. 1992, ApJ, 397, 362
Griest, K., & Safizadeh, N. 1998, ApJ, 500, 37
Han, C., & Gould, A. 1997, ApJ, 480, 196
Han, C., Jung, Y. K., Gould, A., et al. 2023, A&A, 672, A8
Han, C., Bond, I. A., Udalski, A., et al. 2024a, A&A, 691, A237
Han, C., Udalski, A., Bond, I. A., et al. 2024b, A&A, 692, A221
Hodgkin, S. T., Irwin, M. J., Hewett, P. C., & Warren, S. J. 2009, MNRAS, 394, 675
Holtzman, J. A., Watson, A. M., Baum, W. A., et al. 1998, AJ, 115, 1946
Irwin, M. J., Lewis, J., Hodgkin, S., et al. 2004, Proc. SPIE, 5493, 411
Jung, Y. K., Han, C., Gould, A., & Maoz, D. 2013, ApJ, 768, L7
Kervella, P., Thévenin, F., Di Folco, E., & Ségransan, D. 2004, A&A, 426, 29
Kim, S.-L., Lee, C.-U., Park, B.-G., et al. 2016, JKAS, 49, 37
Mao, S., & Paczyński, B. 1991, ApJ, 374, L37
Nataf, D. M., Gould, A., Fouqué, P. et al. 2013, ApJ, 769, 88
Nemiroff, R. J., & Wickramasinghe, W. A. D. T. 1994, ApJ, 424, L21
Paczyński, B. 1986, ApJ, 304, 1
Shvartzvald, Y., Bryden, G., Gould, A., et al. 2017, AJ, 153, 61
Shvartzvald, Y., Calchi Novati, S., Gaudi, B. S., et al. 2018, ApJ, 857, L8
Skowron, J., Udalski, A., Gould, A., et al. 2011, ApJ, 738, 87
Spergel, D., Gehrels, N., Baltay, C., et al. 2015, arXiv e-prints [arXiv:1503.03757]
Sumi, T., Abe, F., Bond, I. A., et al. 2003, ApJ, 591, 204
Udalski, A. 2003, Acta Astron., 53, 291
Udalski, A., Szymański, M. K., & Szymański, G. 2015, Acta Astron., 65, 1
Wen, Y., Zang, W., & Ma, B. 2023, ApJS, 269, 28
Witt, H. J., & Mao, S. 1994, ApJ, 430, 505
Yee, J. C., Shvartzvald, Y., Gal-Yam, A., et al. 2012, ApJ, 755, 102

[1] Department of Physics, Chungbuk National University, Cheongju 28644, Republic of Korea
[2] Center for Astrophysics | Harvard & Smithsonian 60 Garden St., Cambridge, MA 02138, USA
[3] Department of Astronomy, Tsinghua University, Beijing 100084, China
[4] Astronomical Observatory, University of Warsaw, Al. Ujazdowskie 4, 00-478 Warszawa, Poland
[5] Korea Astronomy and Space Science Institute, Daejon 34055, Republic of Korea
[6] Institute of Natural and Mathematical Science, Massey University, Auckland 0745, New Zealand
[7] School of Physics and Astronomy, Sun Yat-sen University, Zhuhai 519082, PR China

[8] CSST Science Center for the Guangdong-Hong Kong-Macau Great Bay Area, Sun Yat-sen University, Zhuhai 519082, China
[9] University of Canterbury, Department of Physics and Astronomy, Private Bag 4800, Christchurch 8020, New Zealand
[10] Department of Astronomy, The Ohio State University, 140 W. 18th Ave., Columbus, OH 43210, USA
[11] School of Space Research, Kyung Hee University, Yongin, Kyeonggi 17104, Republic of Korea
[12] Department of Particle Physics and Astrophysics, Weizmann Institute of Science, Rehovot 76100, Israel
[13] Department of Physics, University of Warwick, Gibbet Hill Road, Coventry CV4 7AL, UK
[14] Villanova University, Department of Astrophysics and Planetary Sciences, 800 Lancaster Ave., Villanova, PA 19085, USA
[15] Institute for Space-Earth Environmental Research, Nagoya University, Nagoya 464-8601, Japan
[16] Code 667, NASA Goddard Space Flight Center, Greenbelt, MD 20771, USA
[17] Department of Astronomy, University of Maryland, College Park, MD 20742, USA
[18] Department of Earth and Planetary Science, Graduate School of Science, The University of Tokyo, 7-3-1 Hongo, Bunkyo-ku, Tokyo 113-0033, Japan
[19] Instituto de Astrofísica de Canarias, Vía Láctea s/n, 38205 La Laguna, Tenerife, Spain
[20] Department of Earth and Space Science, Graduate School of Science, Osaka University, Toyonaka, Osaka 560-0043, Japan
[21] Institute of Astronomy, Graduate School of Science, The University of Tokyo, 2-21-1 Osawa, Mitaka, Tokyo 181-0015, Japan
[22] Oak Ridge Associated Universities, Oak Ridge, TN 37830, USA
[23] Institute of Space and Astronautical Science, Japan Aerospace Exploration Agency, 3-1-1 Yoshinodai, Chuo, Sagamihara, Kanagawa 252-5210, Japan
[24] Sorbonne Université, CNRS, UMR 7095, Institut d'Astrophysique de Paris, 98 bis bd Arago, 75014 Paris, France
[25] Department of Physics, University of Auckland, Private Bag 92019, Auckland, New Zealand
[26] University of Canterbury Mt. John Observatory, P.O. Box 56, Lake Tekapo 8770, New Zealand